

Simulating bulk viscosity in neutron stars II: evolution in spherical symmetry

Giovanni Camelio,¹ Lorenzo Gavassino,¹ Marco Antonelli,^{2,1} Sebastiano Bernuzzi,³ and Brynmor Haskell¹

¹*Nicolaus Copernicus Astronomical Center, Polish Academy of Science, Bartycka 18, 00-716 Warsaw, Poland*

²*CNRS/IN2P3, ENSICAEN, Laboratoire de Physique Corpusculaire, 14000 Caen, France*

³*Theoretisch-Physikalisches Institut, Friedrich-Schiller-Universität Jena, 07743, Jena, Germany*

(Dated: April 26, 2022)

Out-of-equilibrium reactions between different particle species are the main process contributing to bulk viscosity in neutron stars. In this work, we numerically compare three different approaches to the modeling of bulk viscosity: the multi-component fluid with reacting particle species and two bulk stress formalism based on the Müller-Israel-Stewart theory, namely the Hiscock-Lindblom and the Maxwell-Cattaneo models, whose flux-conservative formulation in radial gauge-polar slicing coordinates and spherical symmetry is derived in a companion paper. In our knowledge, this is the first time that a neutron star is simulated with the complete Hiscock-Lindblom model of bulk viscosity. We find that the Hiscock-Lindblom and Maxwell-Cattaneo models are good approximations of the multi-component fluid for small perturbations and when the non-equilibrium equation of state of the fluid depends on only one independent particle fraction. For more than one independent particle fraction and for large perturbations, the bulk stress approximation is still valid but less accurate. In addition, we include the energy loss due to the luminosity of the reactions in the bulk stress formulation. We find that the energy loss due to bulk viscosity has a larger effect on the dynamics than the bulk stress or the variation in particle composition *per se*. The new one-dimensional, general-relativistic hydrodynamic code developed for this work, **hydro-bulk-1D**, is publicly available.

I. INTRODUCTION

Recent advances in fields as diverse as gravitational wave astronomy and heavy ion collisions have lead to a renewed interest in relativistic formulations of dissipative hydrodynamics, as experiments and observations become sensitive enough to probe these effects [1–3].

In neutron star simulations the effects of shear viscosity, which is expected to play a strong role as magneto-hydrodynamic turbulence develops after a neutron star merger, have been considered by few authors [4–10], while bulk viscosity has received less attention. Nevertheless, recent studies suggest that the thermodynamic conditions in a neutron star merger may be such that bulk viscosity could be dynamically significant [11–14], even if no clear evidence of this effect has been found in simulations [15–18], see for example the introductory discussion in our companion paper [19].

Bulk viscosity is an out-of-equilibrium dissipative process, which in neutron stars is mostly due to particle reactions, and in particular to the so-called Urca processes [11]. Bulk viscosity in neutron stars may impact on several aspects of their dynamics. For example, it determines the damping time-scale of radial oscillations which have been excited at the time of the proto-neutron star formation from supernovae. Viscosity also defines the window for the gravitational wave instabilities in rotating neutron stars [20–22] and thereby the theoretical upper limits on their rotation rates [23].

Many calculations of the bulk-viscosity coefficients arising from different kinds of reactions have been reported in literature, e.g. [11, 24–29]. Recently, there has been a renewed interest in this problem also because bulk viscosity can in principle leave an observable imprint on

the gravitational wave signal emitted during neutron star mergers, even if preliminary studies have found that any effect is probably minor [15–18].

In this work, we numerically compare three different approaches to the modeling of bulk viscosity in neutron stars: the multi-component fluid with tracking of the reacting particle species [30], and two bulk stress formalism based on the Müller-Israel-Stewart theory [31], namely the Hiscock-Lindblom [32] and the Maxwell-Cattaneo [33] models, whose flux-conservative formulation in radial gauge-polar slicing coordinates and spherical symmetry is discussed in the companion paper [19]. To our knowledge, this is the first implementation of Müller-Israel-Stewart theories in radial gauge-polar slicing coordinates in spherical symmetry and the first implementation of the complete Hiscock-Lindblom model in the context of neutron stars. We find that the bulk stress formalism (i.e., Hiscock-Lindblom and Maxwell-Cattaneo) is a good approximation of the multi-component fluid for small perturbations and for one independent particle fraction (namely, when we can select the electron fraction as the only independent fraction variable of the equation of state). For more than one independent fraction variable in the equation of state, the bulk stress approximation is still valid but loses accuracy¹. In addition, we include for the first time the energy loss due to the reaction luminosity in the bulk stress formulations [19], finding that its inclusion influences the dynamics more

¹ When the viscous degrees of freedom are doubled, the relaxation-time approximation may no longer be valid [34]. Sometimes, this can lead to exotic dynamics, which cannot be described within the Müller-Israel-Stewart formalism [35].

than the bulk stress alone.

In order to perform this study, we developed ‘hydro-bulk-1D’, a new one dimensional general relativistic hydrodynamic code. We publicly release [36] hydro-bulk-1D on `zenodo` under the MIT license to allow the community to check and improve our results.

This paper is organized as follows. In Sec. II we describe the bulk viscous models and the hydrodynamic equations. In Sec. III we describe the equation of state and the reaction rates. In Sec. IV we introduce the code. In Sec. V we compare the different approaches to bulk viscosity. We draw our conclusions in Sec. VI. We describe in detail the numerical implementation of the code in Appendix A and we perform a set of standard tests in Appendix B.

We adopt the $(-, +, +, +)$ metric signature and, unless otherwise specified, we set $c = G = M_\odot = k_B = 1$, which are our code units. In these units, the rest mass saturation density is $\rho_n \simeq 4.34 \times 10^{-4}$, one kilometer is $\text{km} \simeq 0.677$, and one millisecond is $\text{ms} \simeq 203$.

II. HYDRODYNAMIC MODEL

We briefly recall some defining properties of the three approaches to bulk viscosity that we implement in our numerical simulations. More details are given in the companion paper [19]. Then, we specify their hydrodynamic equations in radial gauge-polar slicing coordinates and spherical symmetry.

A. Bulk viscosity: three approaches

We consider 3 different approaches to bulk viscosity: (i) the multi-component fluid with the tracking of the chemical reactions and particle abundances, and two Müller-Israel-Stewart theories, namely (ii) the Hiscock-Lindblom theory, and (iii) the Maxwell-Cattaneo theory, see Camelio et al. [19].

As long as the fluid elements are isotropic (e.g., in the absence of heat, superfluid or electric currents), the stress-energy tensor for the three models (i)-(iii) can be written as:

$$T^{\mu\nu} = (\epsilon + p)u^\mu u^\nu + pg^{\mu\nu}, \quad (1)$$

where u^μ is the 4-velocity of the fluid and $g^{\mu\nu}$ is the metric. The physical meaning of the pressure p depends on the model considered: for the multi-component fluid (i) it is $p = p(\rho, \epsilon, \{Y_i\}_i)$, while for the Müller-Israel-Stewart theories (ii)-(iii) it is $p = p^{\text{eq}}(\rho, \epsilon) + \Pi$. Above, we call ρ the rest mass density, $Y_i = \rho_i/\rho$ the particle fraction of species i (ρ_i is the rest mass density of particle i), Π the bulk stress, and the ‘eq’ superscript refers to quantities in beta-equilibrium.

Note that Y_i and Π are independent variables that have their own dynamics in models (i) and (ii)-(iii), respec-

tively, and in order to evolve the system we need to provide an equation for them. For the multi-component fluid the evolution of each chemical fractions Y_i is given by the corresponding continuity equation:

$$\nabla_\mu(\rho Y_i u^\mu) = m_n \mathcal{R}_i, \quad (2)$$

where m_n is the neutron mass and \mathcal{R}_i is the net reaction rate of particle species i . In the Hiscock-Lindblom model, the additional equation for the bulk stress is:

$$\nabla_\mu(\Pi u^\mu) = -\frac{\Pi}{\tau} - \left(\frac{1}{\chi} - \frac{\Pi}{2}\right) \nabla_\mu u^\mu - \frac{\Pi}{2} u^\mu \nabla_\mu \left(\log \frac{\chi}{T^{\text{eq}}}\right), \quad (3)$$

where χ is the bulk viscous parameter, τ is the bulk viscous timescale, and T^{eq} is the temperature in beta-equilibrium. Finally, Maxwell-Cattaneo is a linearization of Hiscock-Lindblom, and for it the additional equation that describes the evolution of the bulk stress is:

$$\nabla_\mu(\Pi u^\mu) = -\frac{\Pi}{\tau} - \left(\frac{1}{\chi} - \Pi\right) \nabla_\mu u^\mu. \quad (4)$$

B. From the multi-component fluid to Müller-Israel-Stewart

For small deviations from equilibrium, we can derive an equivalent Müller-Israel-Stewart description of bulk viscosity from the multi-component fluid one, thanks to the relations [19, 37, 38]:

$$\zeta = n^4 \Xi^{ab} \frac{\partial Y_a^{\text{eq}}}{\partial n} \bigg|_s \frac{\partial Y_b^{\text{eq}}}{\partial n} \bigg|_s, \quad (5)$$

$$\Xi_{ab} = \frac{\partial \mathcal{R}_a(\{\mathbb{A}^j = 0\}_{\forall j})}{\partial \mathbb{A}^b} \bigg|_{\rho, s, \{\mathbb{A}^i\}_{i \neq b}}, \quad (6)$$

$$\Pi = \mathbb{A}^i \frac{\partial Y_i^{\text{eq}}}{\partial n} \bigg|_s n^2, \quad (7)$$

where $n = \rho/m_n$ is the baryon number density, s the entropy per baryon, \mathbb{A}^i the affinity of particle i , and the a, b indices refer to the particle species (e.g., $\{e, \mu\}$), are summed with the Einstein rule, and are raised and lowered with matrix inversion ($\Xi_{ab} \Xi^{bc} = \mathbb{I}$). The bulk viscous timescale τ and the bulk viscous parameter χ are, strictly speaking, defined only for one independent species,

$$\tau = -\frac{n}{\Xi} \frac{\partial Y(\mathbb{A} = 0)}{\partial \mathbb{A}} \bigg|_{\rho, s}, \quad (8)$$

$$\chi = \frac{\tau}{\zeta}, \quad (9)$$

where $\Xi = \Xi_{11}$ and we dropped the species index because there is only one independent species. However, we can extend this formulation to more than one independent species requiring that the speed of sound of the

multi-component fluid coincides with that of the Müller-Israel-Stewart theories for small perturbation from thermodynamic equilibrium [19]:

$$\tau = \frac{n\Xi^{ab} \frac{\partial Y_a^{\text{eq}}}{\partial \rho} \Big|_s \frac{\partial Y_b^{\text{eq}}}{\partial \rho} \Big|_s}{m_n \frac{\partial^2 u}{\partial Y_c \partial Y_d} \Big|_{\rho, s} \frac{\partial Y_c^{\text{eq}}}{\partial \rho} \Big|_s \frac{\partial Y_d^{\text{eq}}}{\partial \rho} \Big|_s}. \quad (10)$$

C. Including luminosity

For all the three models (i)-(iii), the total rest mass density satisfies the continuity equation

$$\nabla_\mu (\rho u^\mu) = 0, \quad (11)$$

and the stress-energy tensor evolution is given by the usual momentum and energy conservation equations²:

$$\nabla_\mu (T^{\mu\nu}) = -Q u^\nu, \quad (12)$$

where Q is the total luminosity. For the multi-component fluid, $Q = \sum_j Q_j$, where Q_j is the luminosity of reaction j . In Müller-Israel-Stewart theories, the energy luminosity is usually neglected, $Q = 0$. However, in the companion paper [19] we show that it is possible to account for the energy luminosity also in this kind of theories by performing an expansion around equilibrium:

$$Q(\rho, s, \Pi) = Q^{\text{eq}}(\rho, s^{\text{eq}}) + \frac{\partial Q}{\partial \Pi} \Pi + \mathcal{O}(\Pi^2), \quad (13)$$

$$\frac{\partial Q}{\partial \Pi} = \frac{1}{n^2} \left(\frac{\partial Y^{\text{eq}}}{\partial n} \Big|_s \right)^{-1} \frac{\partial Q(\Lambda = 0)}{\partial \Lambda} \Big|_{\rho, s}, \quad (14)$$

where, for simplicity, the above formula refers to the particular case in which there is a single independent fraction Y in the non-equilibrium equation of state of the corresponding multi-component fluid, $\epsilon = \epsilon(\rho, s, Y)$.

D. Hydrodynamic equations in radial gauge, polar slicing coordinates in spherical symmetry

We adopt the radial gauge, polar slicing coordinates in spherical symmetry (i.e. Schwarzschild), whose metric is:

$$dl^2 = -\alpha^2(r, t) dt^2 + X^2(r, t) dr^2 + r^2 d\Omega^2, \quad (15)$$

where l is the proper time, t and r are respectively the time and radial coordinates, $d\Omega$ is the angular element, α is the lapse function:

$$\alpha(r, t) = \exp(\phi(r, t)), \quad (16)$$

the metric function X is given by:

$$X(r, t) = \left(1 - \frac{2m(r, t)}{r} \right)^{-1/2}, \quad (17)$$

m is the gravitational mass:

$$m(r, t) = 4\pi \int_0^r ((\epsilon + p)W^2 - p)x^2 dx, \quad (18)$$

ϕ is the general relativistic equivalent of the Newtonian gravitational field:

$$\phi(r, t) = \int_0^r X^2 \left(\frac{m}{x^2} + 4\pi x((\epsilon + p)W^2 v^2 + p) \right) dx + \phi_0, \quad (19)$$

W is the Lorentz factor:

$$W = (1 - v^2)^{-1/2}, \quad (20)$$

v is the velocity of the fluid, and the integration constant ϕ_0 is determined by the condition $\phi \rightarrow 0$ as $r \rightarrow \infty$, from which we obtain:

$$\phi(r > R, t) = \frac{1}{2} \log \left(1 - \frac{2m(R, t)}{r} \right), \quad (21)$$

where R is the stellar radius. Finally, the total baryon mass of the star is:

$$M_b = 4\pi \int_0^R X \rho W x^2 dx. \quad (22)$$

In radial gauge, polar slicing coordinates in spherical symmetry, the continuity equations reads [39, 40]:

$$\partial_t D + \frac{1}{r^2} \partial_r \left(\frac{\alpha r^2}{X} D v \right) = 0, \quad (23)$$

$$D = X \rho W, \quad (24)$$

the momentum conservation equation reads [39, 40]:

$$\begin{aligned} \partial_t S^r + \frac{1}{r^2} \partial_r \left(\frac{\alpha r^2}{X} (S^r v + p) \right) &= -\alpha W v Q \\ &- \epsilon \alpha X \left(8\pi r p + \frac{m}{r^2} \right) + \alpha X p \frac{m}{r^2} + \frac{2\alpha p}{X r}, \end{aligned} \quad (25)$$

$$S^r = (\epsilon + p)W^2 v, \quad (26)$$

the energy conservation equation reads [39, 40]:

$$\partial_t \tau_\epsilon + \frac{1}{r^2} \partial_r \left(\frac{\alpha r^2}{X} (S^r - D v) \right) = -\alpha W Q, \quad (27)$$

$$\tau_\epsilon = (\epsilon + p)W^2 - p - D, \quad (28)$$

the particle continuity equation reads [39]:

$$\partial_t (D Y_i) + \frac{1}{r^2} \partial_r \left(\frac{\alpha r^2}{X} D Y_i v \right) = \alpha X m \mathcal{R}_i, \quad (29)$$

² Here we assume that neutrinos are emitted isotropically in the fluid rest frame and immediately leave the star. See Appendix A of O'Connor and Ott [39] for a more general setting.

the bulk stress equation in the Hiscock-Lindblom theory reads [19]:

$$\begin{aligned} \partial_t(XW\Pi) + \frac{1}{r^2}\partial_r(r^2\alpha Wv\Pi) = & -\frac{\alpha X\Pi}{\tau} \\ & -\left(\frac{1}{\chi} - \frac{\Pi}{2}\right)\left(\partial_t(XW) + \frac{1}{r^2}\partial_r(r^2\alpha Wv)\right) \\ & -\frac{\Pi W}{2}\left(X\partial_t\log\frac{\chi}{T^{\text{eq}}} + \alpha v\partial_r\log\frac{\chi}{T^{\text{eq}}}\right), \end{aligned} \quad (30)$$

and the bulk stress equation in the Maxwell-Cattaneo theory reads [19]:

$$\begin{aligned} \partial_t(XW\Pi) + \frac{1}{r^2}\partial_r(r^2\alpha Wv\Pi) = & -\frac{\alpha X\Pi}{\tau} \\ & -\left(\frac{1}{\chi} - \Pi\right)\left(\partial_t(XW) + \frac{1}{r^2}\partial_r(r^2\alpha Wv)\right), \end{aligned} \quad (31)$$

where as above it is $p = p(\rho, \epsilon, \{Y_i\}_i)$ for the multi-component fluid and $p = p^{\text{eq}}(\rho, \epsilon) + \Pi$ for Hiscock-Lindblom and Maxwell-Cattaneo.

III. MICROPHYSICS

Here we summarize the microscopic input needed for our numerical simulations. For a more detailed discussion, see the companion paper [19].

A. Reaction rates and luminosity

We consider a neutrino-less fluid of neutrons ‘n’, protons ‘p’, electrons ‘e’, and muons ‘μ’, that undergoes direct beta reactions:

$$\beta_e^- : \quad n \rightarrow p + e^- + \bar{\nu}_e, \quad (32)$$

$$\beta_e^+ : \quad p + e^- \rightarrow n + \nu_e, \quad (33)$$

$$\beta_\mu^- : \quad n \rightarrow p + \mu^- + \bar{\nu}_\mu, \quad (34)$$

$$\beta_\mu^+ : \quad p + \mu^- \rightarrow n + \nu_\mu. \quad (35)$$

Such a fluid is well suited to describe relatively cold neutron stars, but our model can be easily adapted to other cases. The net number reaction rate for the particle $i = \{e, \mu\}$, which is responsible for the change in the particle fraction [see Eq. (29)], due to neutron decay [Eqs. (32) and (34)] and lepton capture [Eqs. (33) and (35)] and linearized around equilibrium in the affinity \mathbb{A}^i , is [19]:

$$\mathcal{R}_i = \frac{8.86 \times 10^{31}}{\text{cm}^3 \text{s}} \sqrt[3]{\frac{Y_i^{\text{eq}} \rho}{\rho_n}} \left(\frac{T^{\text{eq}}}{10^9 \text{K}}\right)^5 \frac{17\pi^4}{30} \frac{\mathbb{A}^i}{k_B T}. \quad (36)$$

We chose to linearize the reaction rates in order to simplify the implementation of the implicit step (See Appendix A). The reaction luminosity linearized around equilibrium in $\Delta Y_i = Y_i - Y_i^{\text{eq}}$ [which in our case is linear

in the affinity \mathbb{A}^i , see Eq. (46)], which is responsible for the change in the energy and momentum of the fluid [see Eqs. (25) and (27)], is [19]:

$$\mathcal{Q}_i = \frac{1.22 \times 10^{25}}{\text{erg}^{-1} \text{cm}^3 \text{s}} \sqrt[3]{\frac{Y_i^{\text{eq}} \rho}{\rho_n}} \left(\frac{T^{\text{eq}}}{10^9 \text{K}}\right)^6 \frac{457\pi^6}{1260} \left(1 + \frac{\Delta Y_i}{3Y_i^{\text{eq}}}\right), \quad (37)$$

where ρ_n is the rest mass density at nuclear saturation.

B. Analytic non-equilibrium equation of state

We assume an analytic equation of state (EOS) for matter out of beta-equilibrium, defined by:

$$u = k_0 \rho + k_{\text{th}} s^2 \rho^{\Gamma_{\text{th}}-1} + \sum_i k_i \Delta Y_i^2, \quad (38)$$

$$\Delta Y_i = Y_i - Y_i^0 \frac{\rho}{\rho_n}, \quad (39)$$

where i is the index of the independent particle fractions (e.g., $i = e, \mu$ in out-of-equilibrium npeμ matter). In the above expression, $u = u(\rho, s, \{Y_i\}_i) = \epsilon/\rho - 1$ is the specific (per unit mass) internal energy, k_0, k_{th}, k_i are constant positive coefficients, Γ_{th} is the thermal polytropic exponent, and Y_i^0 the equilibrium net particle fraction at nuclear saturation. This EOS is a simple extension of a cold $\Gamma = 2$ polytropic EOS; the thermal component was already introduced in Camelió et al. [41]. The dependence on ρ of the cold and particle components of the EOS was chosen [19] such that the pressure and the speed of sound are positive if $Y_i \in [0, 1]$ and

$$k_0 > 2 \sum_i k_i Y_i^0 / \rho_n. \quad (40)$$

Our EOS has the advantages to be simple and analytic, and at the same time it reproduces some behaviors of a realistic EOS, and in particular: (i) the cold EOS at equilibrium is a polytrope, (ii) the temperature goes to zero as the entropy goes to zero, and (iii) the free parameters $\Gamma_{\text{th}}, k_{\text{th}}, k_e, Y_e^0$ have been chosen in order to fit the GM3 EOS [42, 43], see Table I and plots (a) and (b) of Fig. 1.

However, we are not trying to accurately reproduce an existing EOS, as for example the polytropic parameters for the cold GM3 EOS are $\Gamma = 2.88, k_0 = 2.78 \times 10^4$ while we are setting $\Gamma = 2, k_0 = 200$ in order for Eq. (40) to be true.

Given our analytical model for the EOS in (38), the equilibrium value of the particle fractions (obtained in the limit $\mathbb{A}^e = \mathbb{A}^\mu = 0$) is:

$$Y_i^{\text{eq}}(\rho) = Y_i^0 \frac{\rho}{\rho_n} \quad (i = e, \mu). \quad (41)$$

Unfortunately, this expression does not reproduce the correct trend, see plot (c) of Fig. 1. In particular, the equilibrium fraction of muons Y_μ^{eq} deviates noticeably

from the correct trend (see plot (c) of Fig. 1), and as a consequence the contribution of the muons to the dynamics is negligible. Since we are not aiming for an accurate physical description but rather to clarify the role of bulk viscosity in simulations, we decided to artificially enhance the role of muons in the dynamics by modifying their parameters, such that condition (40) is respected. In order to do so, we substitute the muons ‘ μ ’ with an artificially modified muon particle that we call ‘x’ to avoid confusion, such that:

$$Y_x^0 k_x = Y_\mu^0 k_\mu, \quad (42)$$

$$Y_x^0 = Y_e^0. \quad (43)$$

In Table I we report the EOSs used in this paper for the different models described in Sec. V. The EOS for the model ‘PF’ (perfect fluid) has both electrons and modified muons at equilibrium, the EOS for model ‘MF’ (multi-component fluid) has electrons out of equilibrium and modified muons at equilibrium, and the EOS for model ‘MF-x’ has both electrons and modified muons out of equilibrium.

The other thermodynamic quantities can be derived from Eq. (38) and the first law of thermodynamics [19]:

$$p = k_0 \rho^2 + (\Gamma_{\text{th}} - 1) k_{\text{th}} s^2 \rho^{\Gamma_{\text{th}}} - 2 \frac{\rho^2}{\rho_n} \sum_i k_i Y_i^0 \Delta Y_i, \quad (44)$$

$$T = 2m_n k_{\text{th}} s \rho^{\Gamma_{\text{th}} - 1}, \quad (45)$$

$$\mathbb{A}^i = -2m_n k_i \Delta Y_i, \quad (46)$$

$$c_{\text{s,uv}}^2 = \frac{\frac{\partial p^{\text{eq}}}{\partial \rho} \Big|_s - 2 \frac{\rho}{\rho_n} \sum_i k_i Y_i^0 \left(2 \Delta Y_i - Y_i^0 \frac{\rho}{\rho_n} \right)}{\frac{\partial \epsilon^{\text{eq}}}{\partial \rho} \Big|_s + \sum_i k_i \Delta Y_i \left(\Delta Y_i - 2 Y_i^0 \frac{\rho}{\rho_n} \right)}, \quad (47)$$

$$c_{\text{s,ir}}^2 = \frac{\partial p^{\text{eq}}}{\partial \rho} \Big|_s \div \frac{\partial \epsilon^{\text{eq}}}{\partial \rho} \Big|_s, \quad (48)$$

$$\frac{\partial p^{\text{eq}}}{\partial \rho} \Big|_s = 2k_0 \rho + \Gamma_{\text{th}} (\Gamma_{\text{th}} - 1) k_{\text{th}} s^2 \rho^{\Gamma_{\text{th}} - 1}, \quad (49)$$

$$\frac{\partial \epsilon^{\text{eq}}}{\partial \rho} \Big|_s = 1 + 2k_0 \rho + \Gamma_{\text{th}} k_{\text{th}} s^2 \rho^{\Gamma_{\text{th}} - 1}, \quad (50)$$

where $c_{\text{s,ir}}$ and $c_{\text{s,uv}}$ are respectively the ‘infrared’ (where the chemical composition is always at equilibrium [19]) and ‘ultraviolet’ speeds of sound [19] (where the thermodynamic derivatives are performed at constant composition [19]), and the ‘eq’ superscript means that the quantity is taken at equilibrium ($\{Y_i = Y_i^{\text{eq}}\}_i$).

TABLE I: Parameters of the EOSs used in this paper. In the last row we report if the parameter has been determined with a fit of the GM3 EOS or if it has been chosen ad-hoc (see text). The equilibrium temperature at saturation density and $s = 4$ is $T^{\text{eq}}(\rho_n, 4 k_B) = 56 \text{ MeV}/k_B$ for all EOSs.

model	k_0	Γ_{th}	k_{th}	k_e	Y_e^0	k_x	Y_x^0
PF	200	1.52	0.374	-	-	-	-
MF	200	1.52	0.374	0.603	0.0570	-	-
MF-x	200	1.52	0.374	0.603	0.0570	0.147	0.0570
	ad-hoc	fit	fit	fit	fit	ad-hoc	ad-hoc

For our choice of EOS and reaction rates, we have:

$$\Xi_{ab} = \text{diag}(\Xi_e, \Xi_x), \quad (51)$$

$$\Xi_i = \frac{8.86 \times 10^{31}}{\text{cm}^3 \text{s}} \sqrt[3]{\frac{Y_i^0 \rho^2}{\rho_n^2}} \left(\frac{T}{10^9 \text{ K}} \right)^5 \frac{17\pi^4}{30k_B T}, \quad (52)$$

$$\zeta = n^2 \frac{\rho^2}{\rho_n^2} \sum_i \frac{(Y_i^0)^2}{\Xi_i}, \quad (53)$$

$$\tau = \frac{n}{2m_n} \times \sum_i \frac{(Y_i^0)^2}{\Xi_i} \div \sum_i k_i (Y_i^0)^2, \quad (54)$$

$$c_{\text{s,uv}}^{\text{eq}2} = c_{\text{s,ir}}^2 + \frac{1}{(\epsilon + p^{\text{eq}})\chi}, \quad (55)$$

$$\Pi = -2\rho \sum_i k_i Y_i^{\text{eq}} \Delta Y_i, \quad (56)$$

where $i = \{e, x\}$.

IV. NUMERICAL METHOD

We implemented a new Eulerian, one-dimensional, general-relativistic hydrodynamic code called **hydro-bulk-1D** in the C programming language and release it [36] on **zenodo** under the MIT license, in such a way that the community can check our results and improve on them.

The code uses finite-differences with the method of lines on an evenly spaced grid. The time evolution is performed with a 3rd order IMplicit-EXplicit Runge-Kutta (IMEX-RK) solver [44] and a Courant-Friedrichs-Lewy factor $\text{CFL} = 0.5$. The spatial fluxes are obtained with the LLF (Local Lax-Friedrichs) approximate Riemann solver [45] with 2nd order (piecewise linear) spatial reconstruction of the primitive variables and the MINMOD slope limiter. The gravitational mass is computed by integrating Eqs. (18) and (19) with the trapezoid method. We use as primitive variables ρ , Wv , u with the addition of Y_e and eventually Y_x (in the case of the multi-component fluid), or Π (in the case of Hiscock-Lindblom and Maxwell-Cattaneo). We perform the conservative to primitive inversion using the Brent method to find the root of the conserved momentum, using Wv as independent variable. When the density is smaller than

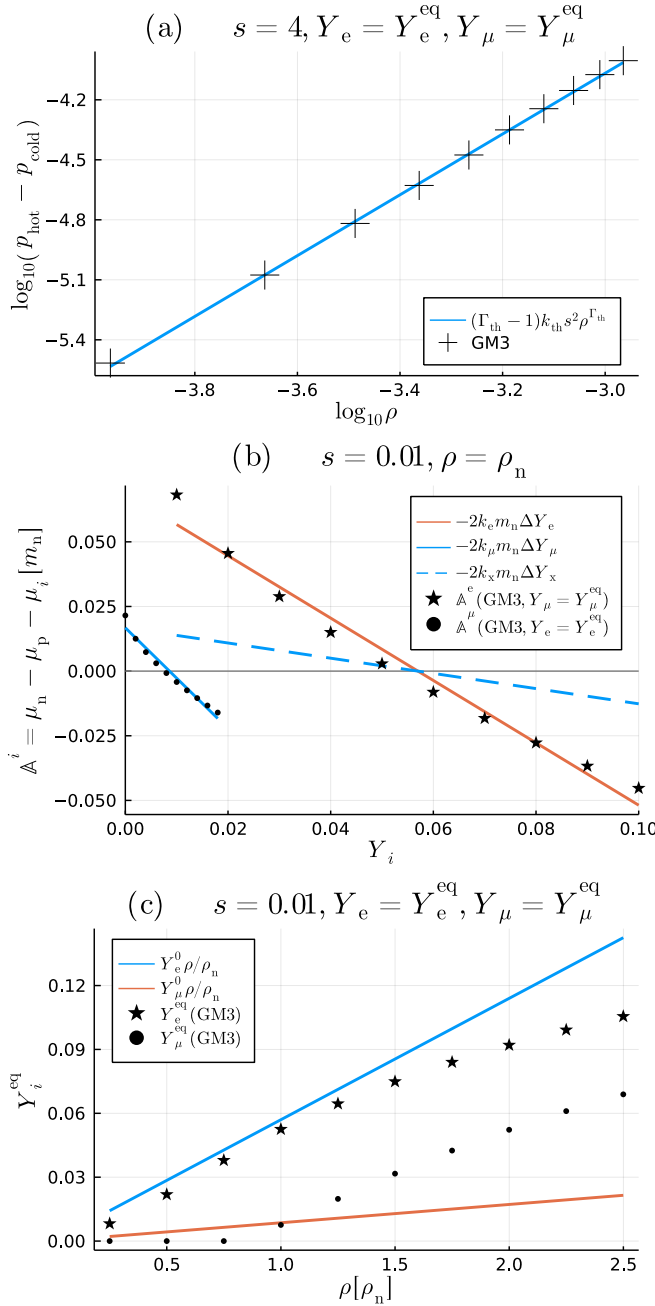


FIG. 1: EOS used in this paper and GM3 EOS. From top to bottom: (a) thermal contribution to the equilibrium pressure (for $s = 4$), (b) dependence of the particle affinity ($\Delta^i = \mu_n - \mu_p - \mu_i$, where $\mu_{\{n,p,i\}}$ are the chemical potentials) on the particle fraction Y_i , (c) dependence of the equilibrium particle fraction on the rest mass density. The value of the muon parameters obtained from the fit are $k_\mu = 0.974$, $Y_\mu^0 = 0.00860$, while the other parameters are reported in Table I.

the threshold value $\rho_{\text{thr}} = 100\rho_{\text{min}}$, we set it as an atmosphere at $\rho_{\text{min}} = 10^{-20}$. In order to avoid division by zero, we set a floor for the temperature at $T_{\text{min}} = 10^{-61}$ (in code units) in the derivative in the source of the Hiscock-Lindblom equation [Eq. (30)]. It is possible to

set in the code a lower order time integration (2nd or 1st) and spatial reconstruction (1st, i.e. piecewise constant), the MCLIM slope limiter [46], and the Harten-Lax-vanLeer (HLL) Riemann-Solver [47].

We adopt an implicit scheme to evolve the equations, as done also by Most and Noronha [48], because the timescale of the reactions can become shorter than the timestep making an explicit method unstable, see also [49] for a recent discussion. Note that bulk stress formulations (namely Hiscock-Lindblom or Maxwell-Cattaneo) do not solve this issue since the bulk viscous timescale τ is related to the reaction timescale.

We describe in more detail the code in Appendix A and we test it in Appendix B.

V. RESULTS

In this section, we compare the bulk viscous evolution performed with different models. For each model, we consider both small deviations (neutron star oscillations) and large deviations (neutron star migration from unstable to stable branch) from hydrostatic equilibrium.

For the oscillation case, we choose as initial condition the stable and isentropic Tolman-Oppenheimer-Volkoff (TOV) model in beta-equilibrium with central density $\rho_0 = 2\rho_n$. The initial uniform entropy per baryon $s = 0.04$ is such that the dissipative timescale in the center is of the order of 1 ms, which is also the order of magnitude of the oscillation period. For this model, $R = 18.7$ km, $M = 2.16 M_\odot$, and $M_b = 2.35 M_\odot$. The other settings specific for the oscillation case are $R_{\text{max}} = 13$, $N = 800$, and $v_{\text{pert}} = 5 \times 10^{-3}$ (v_{pert} determines the amplitude of the initial velocity perturbation), see Appendix A for details. For the migration case, we choose as initial condition the unstable cold ($s = 0$) TOV model in beta-equilibrium with central density $\rho_0 = 4 \times 10^{-3} \simeq 9.22\rho_n$, which gives a star with $R = 12.2$ km, $M = 2.05 M_\odot$, and $M_b = 2.17 M_\odot$. The other settings specific for the migration model are $R_{\text{max}} = 80$, $N = 8001$ ($dr = 0.01$), and $v_{\text{pert}} = 0$. The other settings common to both models are described in Sec. IV, while the EOSs are described in Sec. III. In Fig. 2 we plot the dependence of the total baryon and gravitational masses on the central density of the cold TOV model and we mark the central densities of the oscillation and migration models. We remark that, contrary to the oscillation and migration models considered in the tests (see Appendix B), the two configurations do not have the same baryon number, namely the end result of the migration is not equivalent to the oscillation model.

For each case (oscillations and migration), we will consider 8 different models:

- PF: perfect fluid with all reactions at equilibrium (namely no viscosity and no independent particle fractions),
- MF: multi-component fluid with only electron beta

reactions out of equilibrium (namely the only independent particle fraction are the electrons) and no luminosity ($\mathcal{Q} = 0$),

- HL: Hiscock-Lindblom with only electron beta reactions out of equilibrium (as MF) and no luminosity ($\mathcal{Q} = 0$),
- MC: Maxwell-Cattaneo with only electron beta reactions out of equilibrium (as MF) and no luminosity ($\mathcal{Q} = 0$),
- MF-Q: multi-component fluid with luminosity and only electron beta reactions out of equilibrium (as MF),
- MC-Q: Maxwell-Cattaneo with luminosity and only electron beta reactions out of equilibrium (as MF).
- MF-x: multi-component fluid with electrons and modified muons ‘x’ beta reactions out of equilibrium and no luminosity ($\mathcal{Q} = 0$),
- MC-x: Maxwell-Cattaneo with electrons and modified muons ‘x’ beta reactions out of equilibrium (as MF-x) and no luminosity ($\mathcal{Q} = 0$).

In Fig. 3 we show the central rest mass density evolution of the oscillation (left) and migration (right) models. In order to enhance the differences between the models, we show the central rest mass density of models PF, MF-Q, and MF in plots (a) and (b) and the difference between the central rest mass densities of the other models and that of models MF and MF-Q in plots (c)-(f).

A. Comparison of the three approaches to bulk viscosity

In this subsection, we compare the three dissipative models MF, HL, and MC, together with the additional model PF (no viscosity) that can be used as a benchmark reference. In all cases, we will assume that the modified muons ‘x’ are in equilibrium, so that the only independent fraction that needs to be evolved is Y_e . We also assume that no energy is emitted during the simulation ($\mathcal{Q} = 0$).

In plots (a) and (c) of Fig. 3 we show the central rest mass density for each model for the oscillating case (i.e., small perturbations). The oscillation of the central density for the models with bulk viscosity (MF, MC, HL) is damped with time, while the oscillation of the non-viscous model (PF) has no visible damping on the timescale of the simulation. All three viscous models evolve very similarly, which is a corroboration for the chemical reactions-bulk viscosity correspondence [37] and for the code. However, the HL model is more noisy than MC and MF, due to the additional derivative in the source, since close to the surface both χ and T^{eq}

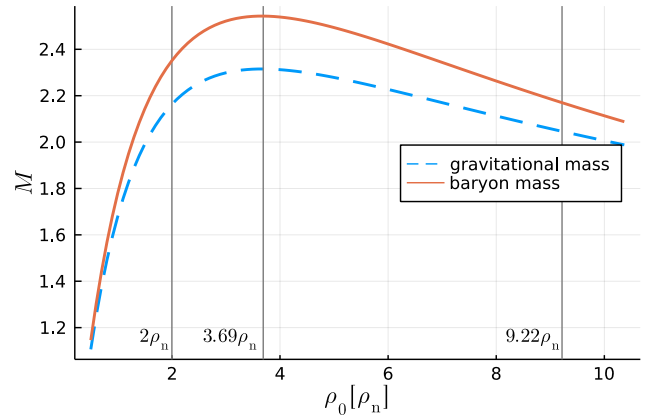


FIG. 2: Central rest mass density vs gravitational and baryon mass for a cold neutron star in chemical equilibrium with the EOS considered in Sec. III ($\Gamma = 2, k_0 = 200$). The vertical lines refer to the oscillating and migration configurations considered in the text (note that the addition of the uniform entropy per baryon $s = 0.04$ does not noticeably change the plot), and to the maximal gravitational mass configuration. The latter separates the stable (left) and the unstable (right) branches and corresponds to $\rho_0 = 3.69\rho_n$, $R = 15.9$ km, $M = 2.32 M_\odot$, and $M_b = 2.54 M_\odot$. The radius of the configuration with $M = 1.4 M_\odot$ for this EOS is $R_{1.4 M_\odot} = 22.5$ km.

reach small values and the quantity $\log(\chi/T^{\text{eq}})$ can become problematic. In order to check how the temperature floor T_{tiny} in the derivative in the source of Eq. (30) influences the evolution, we made some tests varying its value. In Fig. 4 we show the last 5 ms evolution of the central rest mass density (top) and the final temperature profile (bottom) for the oscillating HL model with $T_{\text{tiny}} = \{10^{-65}, 10^{-63}, 10^{-61}\}$. Increasing the value of T_{tiny} reduces the noise in the evolution of the central density because in this way the relative error in the temperature profile is reduced too (note that the truncation error on the temperature is of the order of 10^{-66}). On the other hand, T_{tiny} should be small enough not to overcome the temperature profile. We found that $T_{\text{tiny}} = 10^{-61}$ is a good compromise between reducing the noise and being able to resolve the thermal profile.

In Fig. 5 we plot the value of the bulk stress Π directly evolved with the MC model and that obtained with Eq. (8) from the evolution of the MF model, for the oscillation case. The similarity of the bulk stress obtained with two completely different models is an additional corroboration of the correspondence between the bulk stress theories and the multi-component fluid. As a comparison, the central pressure oscillates around $p \simeq 1.5 \times 10^{-3}$. In the final profile, the pressure is at least 9000 times larger than the absolute value of the bulk stress $|\Pi|$ in most of the star, justifying the bulk stress approximation. However, close to the surface, the bulk stress approaches the pressure and as a consequence the results here lose accuracy.

For large perturbations (migration), the relative con-

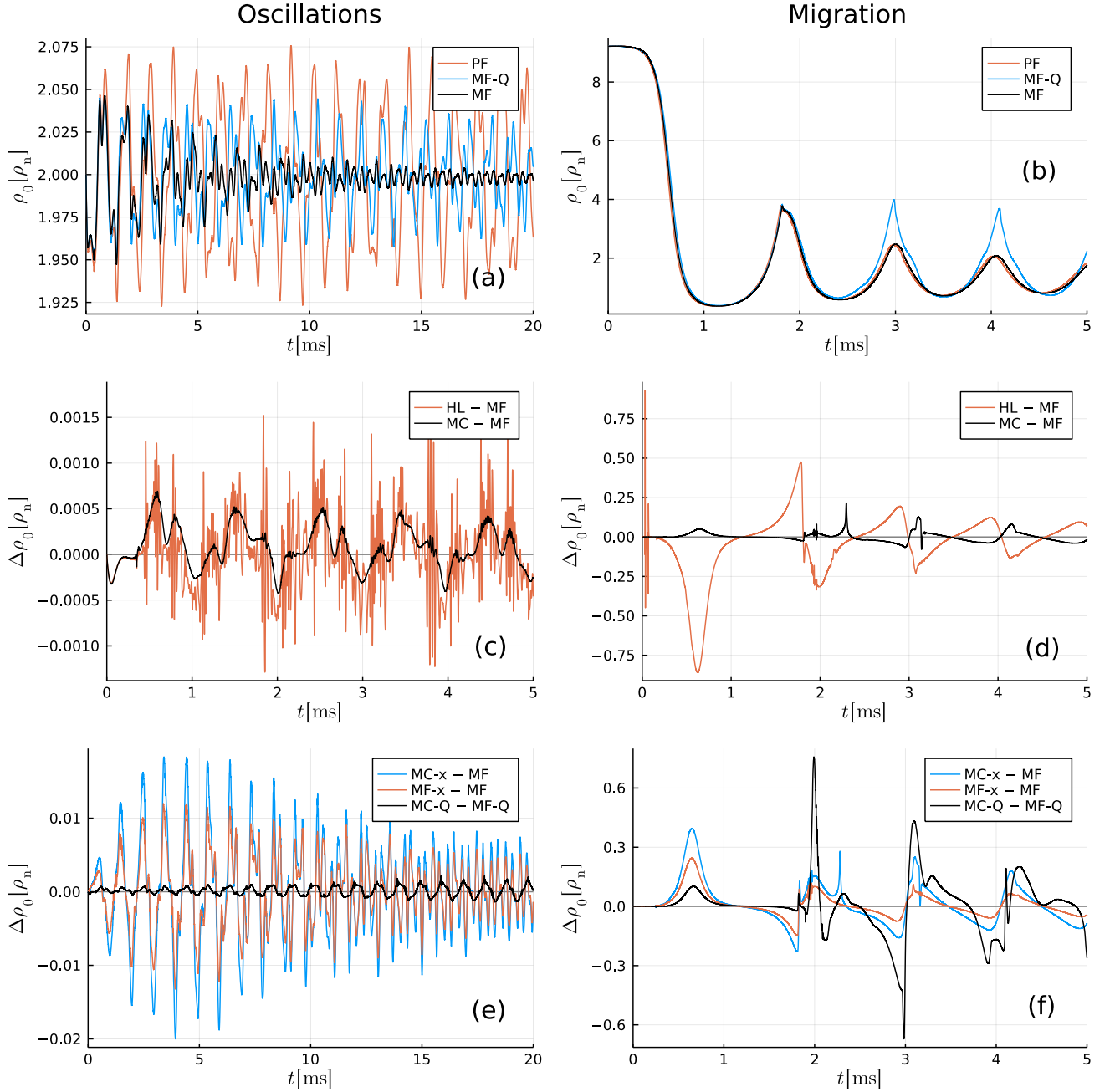


FIG. 3: Evolution of the central rest mass density. On the left [plots (a), (c), and (e)] we show the oscillation case, on the right [plots (b), (d), (f)] we show the migration case. In the first row [plots (a) and (b)] we plot the central rest mass density for the PF, MF, and MF-Q models. In the second and third row, we plot the difference of the central rest mass density between different models. Plot (c) shows a detail of the total evolution, up to 5 ms.

tribution due to bulk viscosity to the dynamics is smaller, see plots (b) and (d) of Fig. 3. The Müller-Israel-Stewart theories reproduce quite well the results of the multi-component fluid, but the approximation is less accurate than in the oscillation case. In Fig. 6 we plot the absolute value of bulk stress $|\Pi|$ directly evolved with the MC and HL models and that obtained with Eq. (8) from the evolution of the MF model, for the migration case.

As in the oscillation case, also for the migration the evolution with the Hiscock-Lindblom model is more noisy than that with the Maxwell-Cattaneo model, and the bulk stress derived from the multi-component fluid with Eq. (8) is very similar to the one evolved with the Müller-Israel-Stewart theories. In the final profile, the pressure is everywhere at least 800 times larger than the absolute value of the bulk stress $|\Pi|$, and hence the bulk stress

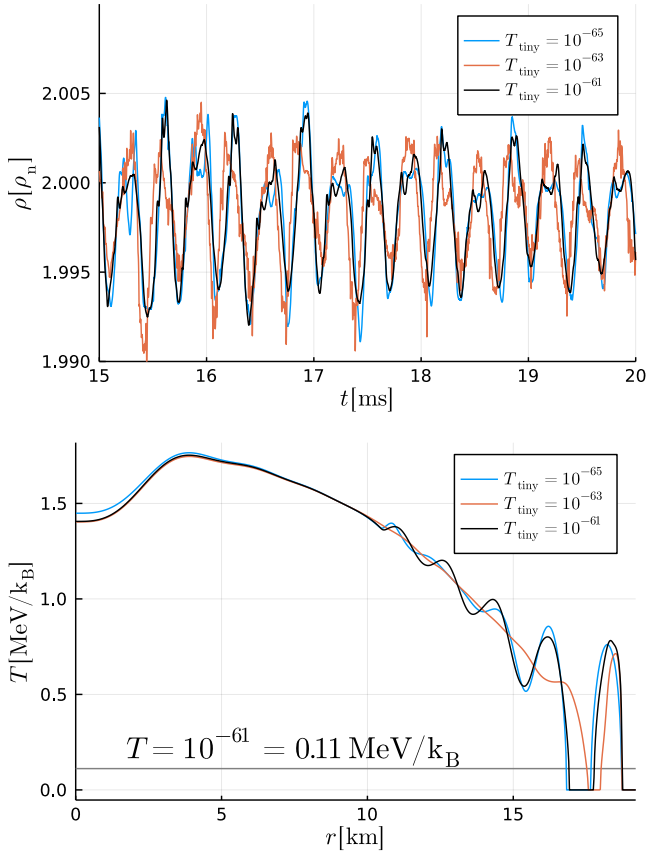


FIG. 4: Dependence of the simulation on the parameter T_{tiny} . On the top, central rest mass density from 15 ms to 20 ms. On the bottom, thermal profile at 20 ms.

approximation is valid.

B. Switching on the luminosity

We now include the luminosity in the evolution. As in the previous subsection, the modified muons ‘x’ are always in beta-equilibrium, so that we only have to evolve Y_e .

As can be seen in plots (e) and (f) of Fig. 3, the central rest mass evolution of the bulk stress model (MC-Q) reproduces very well the multi-component fluid (MF-Q), both for the oscillations and the migration. We also notice that, non-intuitively, the oscillations of the models with luminosity (MF-Q) are larger than in those without (MF), see plots (a) and (b) of Fig. 3. In order to understand this behavior, in Fig. 7 we plotted the central temperature (top) and the time evolution of the temperature profile of the MF-Q model (bottom), for the oscillation (left) and migration (right) cases. The energy extraction occurring in the MF-Q model reduces its temperature with respect to the MF model, which in turn implies that also the number rates [which depend strongly on the temperature, cf. Eq. (36)] are reduced. As a con-

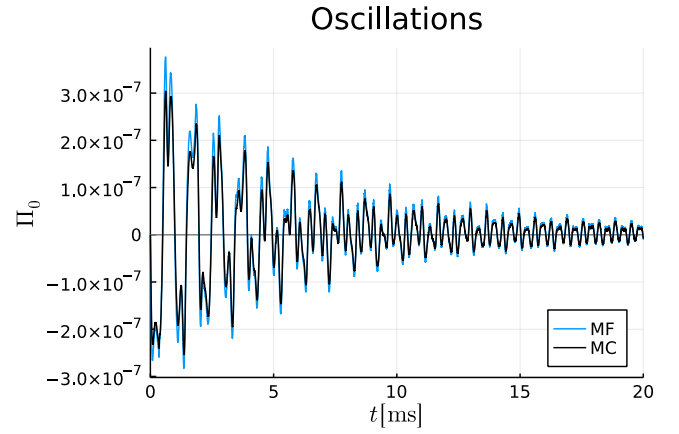


FIG. 5: Bulk stress Π for the oscillating MF and MC models. The bulk stress for the MF model is obtained with Eq. (8). The HL (not shown) and the MC models are very similar.

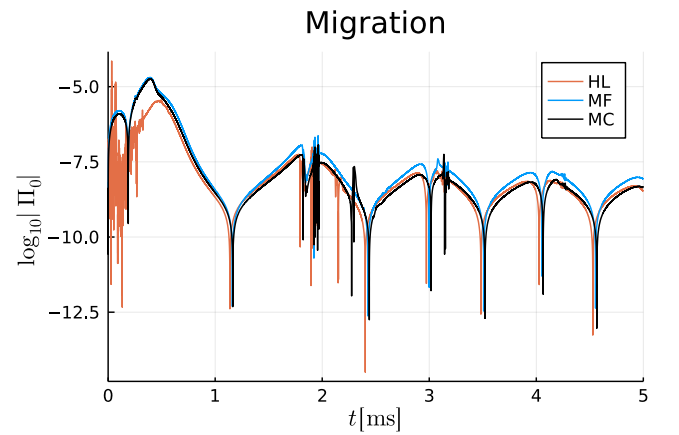


FIG. 6: Bulk stress Π for the migration case. The bulk stress for the MF model is obtained with Eq. (8).

sequence, the particle fractions are allowed to oscillate farther from equilibrium than in the case without luminosity, implying larger deviation from equilibrium of the other thermodynamic quantities. The PF model has no physical viscosity, but due to the always present numerical viscosity there is anyway an increase in the temperature of the star, which is however smaller than that due to the physical bulk viscosity of the MF model (cf. top plots of Fig. 7). The inclusion of luminosity reduces the temperature; for the oscillating case the temperature reduction of the MF-Q model is even smaller than that of PF model.

C. Two independent chemical fractions

Finally, we relax the assumption that there is only one independent particle fraction and we assume that there is no luminosity ($Q = 0$). As mentioned in Sec. III, we modified the parameters of the muons in the EOS in order

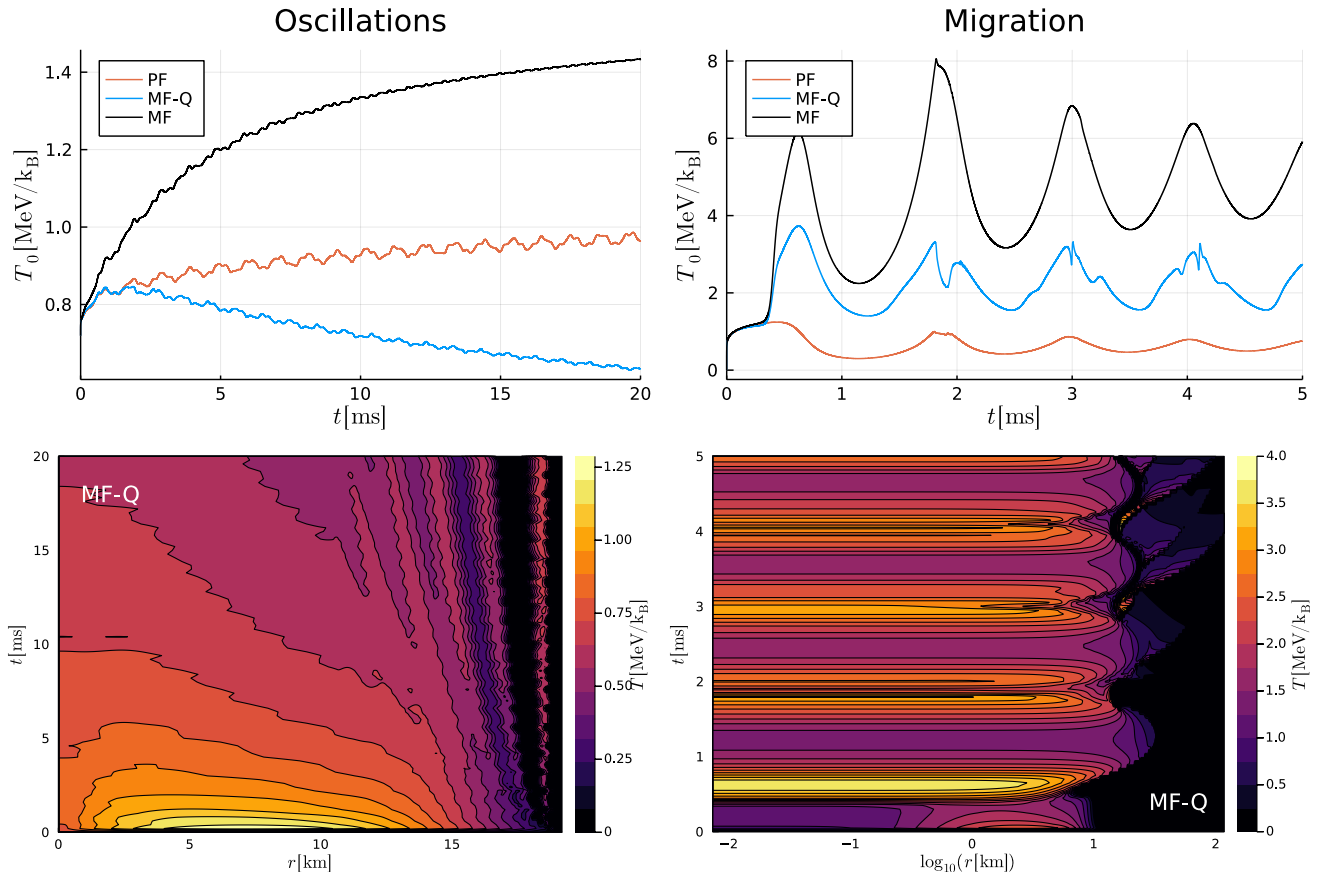


FIG. 7: On the top, central temperature evolution for the PF, MF, and MF-Q models. On the bottom, temperature profile evolution for the MF-Q model. On the left, oscillation case, on the right, migration case.

to enhance their effects on the dynamics. We refer to the modified muons as particle ‘x’.

The difference between the evolution with independent Y_e, Y_x and the evolution with only one independent fraction (Y_e) for the oscillations is shown in plot (e) of Fig. 3. We note that the addition of another degree of freedom (the fraction Y_x) has a limited effect on the dynamics (cfrt. models MF-x, MF, and PF), probably due to the particular choice of the parameters of the EOS. More importantly, the bulk stress approximation for two independent particle fractions is less accurate in describing the bulk viscosity than for one independent particle fraction, cfrt. plots (c) and (e) of Fig. 3. This is due to the fact that the bulk stress correspondence with the multi-component fluid is valid for only one additional independent particle fraction and small perturbations, while in the MC-x model we are considering 2 species out of equilibrium.

For the migration, the results are similar (see plot (f) of Fig. 3), but the bulk stress approximation MC-x of the multi-component fluid MF-x with 2 independent particle species is not appreciably worse than that for one particle species out of equilibrium, cfrt. with models MC and MF in plots (d) and (f) of Fig. 3, probably due to the fact that the loss in accuracy due to the larger deviations from equilibrium overcome that of considering more than one

independent particle fraction.

VI. CONCLUSIONS

In this paper we numerically implement the hydrodynamic equations derived in a companion paper [19]. To do so, we have developed a new one-dimensional, general relativistic, hydrodynamic code called **hydro-bulk-1D** [36]. We use this code to compare different approaches to the inclusion of bulk viscosity in the context of neutron stars, both for small perturbations (oscillations) and large perturbations (migration from unstable to stable branch). In particular, we consider the bulk viscosity caused by beta reactions and we adopt the following approaches: (i) the multi-component fluid, namely the direct tracking of the chemical reactions and the particle species, and two approximations based on the Müller-Israel-Stewart theory, namely (ii) Hiscock-Lindblom, and (iii) Maxwell-Cattaneo, which is a linearization of Hiscock-Lindblom. In our knowledge, this is the first time that the Hiscock-Lindblom formulation has been implemented in the context of neutron stars, and the first time that Müller-Israel-Stewart theories are implemented in radial gauge, polar slicing coordinates in

spherical symmetry. We evolve our model with and without the energy loss due to the luminosity of the reactions and with one (only electrons) or two (both electrons and ‘modified’ muons) species out of equilibrium. The inclusion of the luminosity in the Müller-Israel-Stewart theory is a novel result of the companion paper [19], and this is the first implementation of such extension.

We find that the correspondence between the multi-component description of the fluid and the bulk stress one identified in Gavassino et al. [37] is accurate. The accuracy of the Müller-Israel-Stewart models decreases for more than one independent particle species and for large perturbations (because the mathematical correspondence is no longer rigorous), but they still reproduce correctly the qualitative behavior of the system. However, the Hiscock-Lindblom model is more noisy than the Maxwell-Cattaneo one due to the presence of an additional derivative in the source of Hiscock-Lindblom that involves quantities that are vanishing at the surface.

Our simulations show that the largest effect of bulk viscosity in neutron star dynamics is indirect and due to the energy sink rather than to particle reactions *per se*, because the inclusion of luminosity reduces the temperature of the star, which in turn reduces the reaction rate, and as a consequence the fluid is allowed to oscillate farther from equilibrium. In other words, it is important to correctly include reaction luminosity in the simulations. This can be done also within the bulk stress approach, as shown in this paper and its companion [19].

When the dominant contribution to bulk viscosity in neutron stars comes from chemical reactions, we find that the implementation of the multi-component fluid is more convenient than the bulk stress models. In fact, it is directly and naturally linked to the physics of the system at hand, but it is also capable to accurately describe dissipa-

tion in systems with more than one independent chemical fraction. In addition, its numerical implementation is simpler than that of the Müller-Israel-Stewart models (it has no derivatives in the source). Moreover, contrary to the Müller-Israel-Stewart models that are perturbative, the chemical framework is more robust when the system is driven far from thermodynamic equilibrium [37]. Finally, numerical implementations of a multi-component fluid in the context of neutron stars are much more common and better understood (e.g., supernova simulations) than the ones adopting bulk stress theories.

When bulk viscosity is not directly due to a net imbalance in the direction of chemical reactions, we recommend the use of the Maxwell-Cattaneo model over the Hiscock-Lindblom one, since the latter has an additional derivative in the source that worsen the numerical evolution. In any case, the ratio between the pressure and the bulk stress during the evolution should be monitored, since Müller-Israel-Stewart theories assume the bulk stress to be much smaller than the pressure.

An alternative approach and possible future line of research is to use the correspondence between the multi-component fluid and the bulk stress [37] to derive the equivalent reaction rates from bulk stress parameters, in order to treat the case when bulk viscosity is not due to the presence of non-equilibrium reactions, still using a multi-component fluid. This approach is the inverse of the one adopted in this paper, and it is discussed in [19].

Acknowledgments

This work was supported by the Polish National Science Centre (NCN) grant number OPUS 2019/33/B/ST9/00942. SB acknowledges support by the EU H2020 under ERC Starting Grant, no. BinGraSp-714626.

-
- [1] Paul Romatschke and Ulrike Romatschke. Relativistic Fluid Dynamics In and Out of Equilibrium – Ten Years of Progress in Theory and Numerical Simulations of Nuclear Collisions. *arXiv e-prints*, art. arXiv:1712.05815, December 2017.
 - [2] Wojciech Florkowski, Michal P. Heller, and Michal Spaliński. New theories of relativistic hydrodynamics in the LHC era. *Reports on Progress in Physics*, 81(4): 046001, April 2018. doi: 10.1088/1361-6633/aaa091.
 - [3] Sangwook Ryu, Jean-François Paquet, Chun Shen, Gabriel Denicol, Björn Schenke, Sangyong Jeon, and Charles Gale. Effects of bulk viscosity and hadronic rescattering in heavy ion collisions at energies available at the bnl relativistic heavy ion collider and at the cern large hadron collider. *Phys. Rev. C*, 97:034910, Mar 2018. doi: 10.1103/PhysRevC.97.034910. URL <https://link.aps.org/doi/10.1103/PhysRevC.97.034910>.
 - [4] Kenta Kiuchi, Koutarou Kyutoku, Yuichiro Sekiguchi, and Masaru Shibata. Global simulations of strongly magnetized remnant massive neutron stars formed in binary neutron star mergers. *Phys. Rev. D*, 97(12):124039, June 2018. doi: 10.1103/PhysRevD.97.124039.
 - [5] David Radice. General-relativistic Large-eddy Simulations of Binary Neutron Star Mergers. *ApJ*, 838(1):L2, Mar 2017. doi: 10.3847/2041-8213/aa6483.
 - [6] Masaru Shibata and Kenta Kiuchi. Gravitational waves from remnant massive neutron stars of binary neutron star merger: Viscous hydrodynamics effects. *Phys. Rev. D*, 95(12):123003, June 2017. doi: 10.1103/PhysRevD.95.123003.
 - [7] David Radice, Albino Perego, Kenta Hotokezaka, Sebastiano Bernuzzi, Steven A. Fromm, and Luke F. Roberts. Viscous-dynamical Ejecta from Binary Neutron Star Mergers. *ApJ*, 869(2):L35, Dec 2018. doi: 10.3847/2041-8213/aaf053.
 - [8] Daniele Viganò, Ricard Aguilera-Miret, Federico Car-

- rasco, Borja Miñano, and Carlos Palenzuela. General relativistic MHD large eddy simulations with gradient subgrid-scale model. *Phys. Rev. D*, 101(12):123019, June 2020. doi: 10.1103/PhysRevD.101.123019.
- [9] David Radice. Binary Neutron Star Merger Simulations with a Calibrated Turbulence Model. *Symmetry*, 12(8):1249, 2020. doi: 10.3390/sym12081249.
- [10] Masaru Shibata, Sho Fujibayashi, and Yuichiro Sekiguchi. Long-term evolution of neutron-star merger remnants in general relativistic resistive magnetohydrodynamics with a mean-field dynamo term. *Phys. Rev. D*, 104(6):063026, September 2021. doi: 10.1103/PhysRevD.104.063026.
- [11] P Haensel and R Schaeffer. Bulk viscosity of hot-neutron-star matter from direct urca processes. *Physical review D: Particles and fields*, 45:4708–4712, 07 1992. doi: 10.1103/PhysRevD.45.4708.
- [12] D. G. Yakovlev, A. D. Kaminker, O. Y. Gnedin, and P. Haensel. Neutrino emission from neutron stars. *Phys. Rep.*, 354(1-2):1–155, November 2001. doi: 10.1016/S0370-1573(00)00131-9.
- [13] Andreas Schmitt and Peter Shternin. Reaction Rates and Transport in Neutron Stars. In Luciano Rezzolla, Pierre Pizzochero, David Ian Jones, Nanda Rea, and Isaac Vidana, editors, *Astrophysics and Space Science Library*, volume 457 of *Astrophysics and Space Science Library*, page 455, January 2018. doi: 10.1007/978-3-319-97616-7_9.
- [14] Mark G. Alford, Luke Bovard, Matthias Hanauske, Luciano Rezzolla, and Kai Schwenzer. Viscous Dissipation and Heat Conduction in Binary Neutron-Star Mergers. *Phys. Rev. Lett.*, 120(4):041101, Jan 2018. doi: 10.1103/PhysRevLett.120.041101.
- [15] Albino Perego, Sebastiano Bernuzzi, and David Radice. Thermodynamics conditions of matter in neutron star mergers. *European Physical Journal A*, 55(8):124, Aug 2019. doi: 10.1140/epja/i2019-12810-7.
- [16] Elias R. Most, Steven P. Harris, Christopher Plumberg, Mark G. Alford, Jorge Noronha, Jacquelyn Noronha-Hostler, Frans Pretorius, Helvi Witek, and Nicolás Yunes. Projecting the likely importance of weak-interaction-driven bulk viscosity in neutron star mergers. *arXiv e-prints*, art. arXiv:2107.05094, July 2021.
- [17] P. Hammond, I. Hawke, and N. Andersson. Thermal aspects of neutron star mergers. *Phys. Rev. D*, 104(10):103006, November 2021. doi: 10.1103/PhysRevD.104.103006.
- [18] David Radice, Sebastiano Bernuzzi, Albino Perego, and Roland Haas. A new moment-based general-relativistic neutrino-radiation transport code: Methods and first applications to neutron star mergers. *Monthly Notices of the Royal Astronomical Society*, 512(1):1499–1521, 03 2022. ISSN 0035-8711. doi: 10.1093/mnras/stac589. URL <https://doi.org/10.1093/mnras/stac589>.
- [19] Giovanni Camelo, Lorenzo Gavassino, Marco Antonelli, Sebastiano Bernuzzi, and Brynmor Haskell. Simulating bulk viscosity in neutron stars I: formalism. *in preparation*, 2021.
- [20] Curt Cutler and Lee Lindblom. The Effect of Viscosity on Neutron Star Oscillations. *Astrophys. J.*, 314:234, March 1987. doi: 10.1086/165052.
- [21] Curt Cutler, Lee Lindblom, and Randall J. Splinter. Damping Times for Neutron Star Oscillations. *Astrophys. J.*, 363:603, November 1990. doi: 10.1086/169370.
- [22] Nils Andersson, David Ian Jones, Kostas D. Kokkotas, and Nikolaos Stergioulas. R-Mode Runaway and Rapidly Rotating Neutron Stars. *ApJ*, 534(1):L75–L78, May 2000. doi: 10.1086/312643.
- [23] L. Lindblom. Estimates of the Maximum Angular Velocity of Rotating Neutron Stars. *Astrophys. J.*, 303:146, April 1986. doi: 10.1086/164061.
- [24] P. Haensel, K. P. Levenfish, and D. G. Yakovlev. Bulk viscosity in superfluid neutron star cores. I. Direct Urca processes in npmu matter. *A&A*, 357:1157–1169, May 2000.
- [25] P. Haensel, K. P. Levenfish, and D. G. Yakovlev. Bulk viscosity in superfluid neutron star cores. II. Modified Urca processes in npe mu matter. *A&A*, 372:130–137, June 2001. doi: 10.1051/0004-6361:20010383.
- [26] Mikhail E. Gusakov and Elena M. Kantor. Bulk viscosity of superfluid hyperon stars. *Phys. Rev. D*, 78(8):083006, October 2008. doi: 10.1103/PhysRevD.78.083006.
- [27] P. Haensel, K. P. Levenfish, and D. G. Yakovlev. Bulk viscosity in superfluid neutron star cores. III. Effects of Sigma⁻ hyperons. *A&A*, 381:1080–1089, Jan 2002. doi: 10.1051/0004-6361:20011532.
- [28] Mark G. Alford, Matt Braby, and Andreas Schmitt. Bulk viscosity in kaon-condensed color flavor-locked quark matter. *Journal of Physics G Nuclear Physics*, 35(11):115007, Nov 2008. doi: 10.1088/0954-3899/35/11/115007.
- [29] Mark Alford, Arus Harutyunyan, and Armen Sedrakian. Bulk viscosity from urca processes: npmu matter in the neutrino-trapped regime. *Phys. Rev. D*, 104:103027, Nov 2021. doi: 10.1103/PhysRevD.104.103027. URL <https://link.aps.org/doi/10.1103/PhysRevD.104.103027>.
- [30] Raymond F. Sawyer. Bulk viscosity of hot neutron-star matter and the maximum rotation rates of neutron stars. *Phys. Rev. D*, 39(12):3804–3806, June 1989. doi: 10.1103/PhysRevD.39.3804.
- [31] W. Israel and J.M. Stewart. Transient relativistic thermodynamics and kinetic theory. *Annals of Physics*, 118(2):341 – 372, 1979. ISSN 0003-4916. doi: [https://doi.org/10.1016/0003-4916\(79\)90130-1](https://doi.org/10.1016/0003-4916(79)90130-1). URL <http://www.sciencedirect.com/science/article/pii/0003491679901301>.
- [32] W. A. Hiscock and L. Lindblom. Stability and causality in dissipative relativistic fluids. *Annals of Physics*, 151(2):466–496, January 1983. doi: 10.1016/0003-4916(83)90288-9.
- [33] Mohamed Zakari and David Jou. Equations of state and transport equations in viscous cosmological models. *Phys. Rev. D*, 48:1597–1601, Aug 1993. doi: 10.1103/PhysRevD.48.1597. URL <https://link.aps.org/doi/10.1103/PhysRevD.48.1597>.
- [34] Gabriel S. Denicol, Jorge Noronha, Harri Niemi, and Dirk H. Rischke. Origin of the relaxation time in dissipative fluid dynamics. *Phys. Rev. D*, 83(7):074019, April 2011. doi: 10.1103/PhysRevD.83.074019.
- [35] Michał P. Heller, Romuald A. Janik, Michał Spaliński, and Przemysław Witaszczyk. Coupling Hydrodynamics to Nonequilibrium Degrees of Freedom in Strongly Interacting Quark-Gluon Plasma. *Phys. Rev. Lett.*, 113(26):261601, December 2014. doi: 10.1103/PhysRevLett.113.261601.
- [36] Giovanni Camelo. hydro-bulk-1D, 2022.
- [37] L. Gavassino, M. Antonelli, and B. Haskell. Bulk viscosity in relativistic fluids: from thermodynamics to hydro-

- dynamics. *Classical and Quantum Gravity*, 38(7):075001, April 2021. doi: 10.1088/1361-6382/abe588.
- [38] Lorenzo Gavassino, Marco Antonelli, and Brynmor Haskell. Multifluid Modelling of Relativistic Radiation Hydrodynamics. *Symmetry* 2020, 12(9):1543, September 2020. doi: 10.3390/sym12091543.
- [39] Evan O’Connor and Christian D. Ott. A new open-source code for spherically symmetric stellar collapse to neutron stars and black holes. *Classical and Quantum Gravity*, 27(11):114103, June 2010. doi: 10.1088/0264-9381/27/11/114103.
- [40] Jose V. Romero, Jose M. A. Ibanez, Jose M. A. Marti, and Juan A. Miralles. A New Spherically Symmetric General Relativistic Hydrodynamical Code. *Astrophys. J.*, 462:839, May 1996. doi: 10.1086/177198.
- [41] Giovanni Camelio, Tim Dietrich, Miguel Marques, and Stephan Rosswog. Rotating neutron stars with non-barotropic thermal profile. *Phys. Rev. D*, 100(12):123001, December 2019. doi: 10.1103/PhysRevD.100.123001.
- [42] N. K. Glendenning. Neutron stars are giant hypernuclei? *Astrophys. J.*, 293:470–493, June 1985. doi: 10.1086/163253.
- [43] N. K. Glendenning and S. A. Moszkowski. Reconciliation of neutron-star masses and binding of the Lambda in hypernuclei. *Phys. Rev. Lett.*, 67:2414–2417, October 1991. doi: 10.1103/PhysRevLett.67.2414.
- [44] L. Pareschi and G. Russo. Implicit-explicit Runge-Kutta schemes and applications to hyperbolic systems with relaxation. *arXiv e-prints*, art. arXiv:1009.2757, September 2010.
- [45] Peter D. Lax. Weak solutions of nonlinear hyperbolic equations and their numerical computation. *Communications on Pure and Applied Mathematics*, 7(1):159–193, 1954. doi: <https://doi.org/10.1002/cpa.3160070112>. URL <https://onlinelibrary.wiley.com/doi/abs/10.1002/cpa.3160070112>.
- [46] Bram van Leer. Towards the ultimate conservative difference scheme. iv. a new approach to numerical convection. *Journal of Computational Physics*, 23(3):276–299, 1977. ISSN 0021-9991. doi: [https://doi.org/10.1016/0021-9991\(77\)90095-X](https://doi.org/10.1016/0021-9991(77)90095-X).
- [47] Amiram Harten, Peter Lax, and Bram van Leer. On upstream differencing and godunov-type schemes for hyperbolic conservation laws. *SIAM Rev.*, 25:35–61, 01 1983.
- [48] Elias R. Most and Jorge Noronha. Dissipative magnetohydrodynamics for nonresistive relativistic plasmas: An implicit second-order flux-conservative formulation with stiff relaxation. *Phys. Rev. D*, 104:103028, Nov 2021. doi: 10.1103/PhysRevD.104.103028. URL <https://link.aps.org/doi/10.1103/PhysRevD.104.103028>.
- [49] T. Celora, I. Hawke, P. C. Hammond, N. Andersson, and G. L. Comer. Formulating bulk viscosity for neutron star simulations. *arXiv e-prints*, art. arXiv:2202.01576, February 2022.
- [50] Michail Chabanov, Luciano Rezzolla, and Dirk H. Rischke. General-relativistic hydrodynamics of non-perfect fluids: 3+1 conservative formulation and application to viscous black hole accretion. *MNRAS*, 505(4):5910–5940, August 2021. doi: 10.1093/mnras/stab1384.
- [51] J. D. Bjorken. Highly relativistic nucleus-nucleus collisions: The central rapidity region. *Phys. Rev. D*, 27(1):140–151, January 1983. doi: 10.1103/PhysRevD.27.140.
- [52] L. Del Zanna, V. Chandra, G. Inghirami, V. Rolando, A. Beraudo, A. De Pace, G. Pagliara, A. Drago, and F. Becattini. Relativistic viscous hydrodynamics for heavy-ion collisions with ECHO-QGP. *European Physical Journal C*, 73:2524, August 2013. doi: 10.1140/epjc/s10052-013-2524-5.
- [53] R Maartens. Dissipative cosmology. *Classical and Quantum Gravity*, 12(6):1455–1465, jun 1995. doi: 10.1088/0264-9381/12/6/011. URL <https://doi.org/10.1088/0264-9381/12/6/011>.
- [54] Loren I. Petrich, Stuart L. Shapiro, and Saul A. Teukolsky. Oppenheimer-Snyder collapse in polar time slicing. *Phys. Rev. D*, 33(8):2100–2110, April 1986. doi: 10.1103/PhysRevD.33.2100.
- [55] Luca Baiotti, Sebastiano Bernuzzi, Giovanni Corvino, Roberto de Pietri, and Alessandro Nagar. Gravitational-wave extraction from neutron-star oscillations: Comparing linear and nonlinear techniques. *Phys. Rev. D*, 79(2):024002, January 2009. doi: 10.1103/PhysRevD.79.024002.
- [56] José A. Font, Tom Goodale, Sai Iyer, Mark Miller, Luciano Rezzolla, Edward Seidel, Nikolaos Stergioulas, Wai-Mo Suen, and Malcolm Tobias. Three-dimensional numerical general relativistic hydrodynamics. ii. long-term dynamics of single relativistic stars. *Phys. Rev. D*, 65:084024, Apr 2002. doi: 10.1103/PhysRevD.65.084024. URL <https://link.aps.org/doi/10.1103/PhysRevD.65.084024>.
- [57] Sebastiano Bernuzzi and David Hilditch. Constraint violation in free evolution schemes: Comparing the BSS-NOK formulation with a conformal decomposition of the Z4 formulation. *Phys. Rev. D*, 81(8):084003, April 2010. doi: 10.1103/PhysRevD.81.084003.
- [58] Marcus Thierfelder, Sebastiano Bernuzzi, and Bernd Brügmann. Numerical relativity simulations of binary neutron stars. *Phys. Rev. D*, 84(4):044012, August 2011. doi: 10.1103/PhysRevD.84.044012.

Appendix A: Numerical implementation

In this appendix we discuss the hydro-bulk-1D code [36] in detail.

1. Grid

We use a 1D, evenly spaced, staggered grid with 2 (for the piecewise linear reconstruction) or 1 (for the piecewise constant reconstruction) ghost cells on each side. The position of each grid point is defined by

$$r_i = \left(i - \frac{1}{2}\right) dr, \quad (\text{A1})$$

$$dr = \frac{R_{\max}}{N - 1}, \quad (\text{A2})$$

where R_{\max} is a parameter setting the physical dimension of the grid, $i = 1 \dots N$, and N is the number of grid points (without ghost cells). The ghost cells are filled with symmetry conditions at the center and by linear extrapolation of the primitive quantities at the external boundary.

2. Spatial reconstruction

According to the order of the spatial reconstruction, the primitive variable Q is obtained at the left and right interfaces of the central position between grid points as:

1st: piecewise constant:

$$Q_{i-1/2}^R = Q_i + \mathcal{O}(dr), \quad (\text{A3})$$

$$Q_{i+1/2}^L = Q_i + \mathcal{O}(dr), \quad (\text{A4})$$

2nd: piecewise linear:

$$Q_{i-1/2}^R = Q_i - \frac{r_i - r_{i-1}}{2} \bar{Q}'_i + \mathcal{O}(dr^2) \quad (\text{A5})$$

$$Q_{i+1/2}^L = Q_i + \frac{r_{i+1} - r_i}{2} \bar{Q}'_i + \mathcal{O}(dr^2) \quad (\text{A6})$$

where \bar{Q}'_i is the limited slope. It is necessary to limit the slope to avoid oscillatory solutions. The slope limiter can be set to:

– MINMOD limiter:

$$\bar{Q}'_i = \begin{cases} Q'_- & |Q'_-| \leq |Q'_+| \text{ and } Q'_- \cdot Q'_+ > 0, \\ Q'_+ & |Q'_+| < |Q'_-| \text{ and } Q'_- \cdot Q'_+ > 0, \\ 0 & \text{otherwise,} \end{cases} \quad (\text{A7})$$

– MCLIM limiter (also called MC limiter) [46]:

$$\bar{Q}'_i = \begin{cases} \min(|Q'_-|, |2Q'_-|, |2Q'_+|) \text{sgn}(Q'_-) & Q'_- \cdot Q'_+ > 0, \\ 0 & \text{otherwise,} \end{cases} \quad (\text{A8})$$

where

$$Q' = \frac{Q_{i+1} - Q_{i-1}}{r_{i+1} - r_{i-1}}, \quad (\text{A9})$$

$$Q'_- = \frac{Q_i - Q_{i-1}}{r_i - r_{i-1}}, \quad (\text{A10})$$

$$Q'_+ = \frac{Q_{i+1} - Q_i}{r_{i+1} - r_i}. \quad (\text{A11})$$

The reconstructed state is used to solve the Riemann problem and to compute the spatial derivatives in the source of Eqs. (30) and (31).

3. Riemann solver

The code can use either the HLL or LLF approximate Riemann solvers, which compute the fluxes at the grid interfaces. The HLL Riemann solver is the following:

$$F_{i-1/2} = \begin{cases} F_L & \lambda_- > 0, \\ \frac{\lambda_+ F_L - \lambda_- F_R + \lambda_+ \lambda_- (U_R - U_L)}{\lambda_+ - \lambda_-} & \lambda_- < 0 < \lambda_+, \\ F_R & \lambda_+ < 0, \end{cases} \quad (\text{A12})$$

TABLE II: General form of the Butcher tableau.

$$\begin{array}{c|c} c_j^\mathcal{E} & a_{ij}^\mathcal{E} \\ \hline & b_j^\mathcal{E} \end{array} \quad \begin{array}{c|c} c_j^\mathcal{I} & a_{ij}^\mathcal{I} \\ \hline & b_j^\mathcal{I} \end{array}$$

where F are the fluxes, U the conservative variables, the subscripts L, R refer to the left and right state, respectively, at the center of the cell (namely at $i - 1/2$), and the signal propagation speeds are:

$$\lambda^+ = \max \left(0, \frac{v_L + c_L}{1 + v_L c_L}, \frac{v_R + c_R}{1 + v_R c_R} \right), \quad (\text{A13})$$

$$\lambda^- = \min \left(0, \frac{v_L - c_L}{1 - v_L c_L}, \frac{v_R - c_R}{1 - v_R c_R} \right), \quad (\text{A14})$$

where c is the ‘ultraviolet’ speed of sound [Eqs. (47) and (55)].

The LLF Riemann solver is:

$$F_{i-1/2} = \frac{1}{2} \left(F_L + F_R - \max(|\lambda^+|, |\lambda^-|) (U_R - U_L) \right). \quad (\text{A15})$$

4. Time evolution

The hydrodynamic equations can be written as:

$$\frac{dU}{dt} = \mathcal{E}(U, t) + \mathcal{I}(U, t), \quad (\text{A16})$$

where $\mathcal{E}(U, t)$ includes the contribution from the fluxes and the explicit sources, while $\mathcal{I}(U, t)$ includes the contribution from the implicit sources.

The timestep dt is determined by:

$$dt = \text{CFL} \times \min_i (dr_i / \max(|v_i|, |\lambda_i^+|, |\lambda_i^-|)), \quad (\text{A17})$$

where CFL is the Courant-Friedrichs-Lewy factor.

To numerically integrate Eq. (A16) at a given order, we use IMPLICIT-EXPLICIT Runge Kutta (IMEX RK):

$$U^i = U(t) + dt \sum_{j=1}^{i-1} a_{ij}^\mathcal{E} \mathcal{E}(U^j, t + c_j^\mathcal{E} dt) + dt \sum_{j=1}^i a_{ij}^\mathcal{I} \mathcal{I}(U^j, t + c_j^\mathcal{I} dt), \quad (\text{A18})$$

$$U(t + dt) = U(t) + dt \sum_{j=1}^n b_j^\mathcal{E} \mathcal{E}(U^j, t + c_j^\mathcal{E} dt) + dt \sum_{j=1}^n b_j^\mathcal{I} \mathcal{I}(U^j, t + c_j^\mathcal{I} dt), \quad (\text{A19})$$

where a_{ij}, b_j, c_j are parameters given by the Butcher tableau, see Table II. We report the adopted parameters of the 2nd order IMEX RK in Table III and the 3rd order

TABLE III: Butcher tableau for IMEX RK at 2nd order, with $\gamma = 1 - 1/\sqrt{2}$. Compare with Table 2 of Pareschi and Russo [44].

0	0	0		γ	γ	0
1	1	0		$1 - \gamma$	$1 - 2\gamma$	γ
	1/2	1/2			1/2	1/2

TABLE IV: Butcher tableau for IMEX RK at 3rd order, with $\gamma = 1 - 1/\sqrt{2}$. Compare with Table 5 of Pareschi and Russo [44].

0	0	0	0	γ	γ	0	0
1	1	0	0	$1 - \gamma$	$1 - 2\gamma$	γ	0
1/2	1/4	1/4	0	1/2	$1/2 - \gamma$	0	γ
	1/6	1/6	2/3		1/6	1/6	2/3

IMEX RK in Table IV. When first order integration in time is set, we use an implicit-explicit Euler:

$$U(t + dt) = U(t) + dt\mathcal{E}(U(t), t) + dt\mathcal{I}(U(t + dt), t + dt). \quad (\text{A20})$$

5. Conservative-to-primitive inversion

We choose the quantities ρ, Wv, u as primitive variables, with the addition of $\{Y_i\}_i$ in the case of the multi-component fluid and of Π in the case of Müller-Israel-Stewart theories. For each grid point, we determine the value of the function X from the conservative variables, noting that the integrand of Eq. (18) is equal to $\tau + D$. We then use the Brent method to find the root of the function

$$f(z) = S^r - (\hat{\epsilon} + \hat{p})z\hat{W}, \quad (\text{A21})$$

where z is the independent variable and

$$\hat{W} = \sqrt{1 + z^2}, \quad (\text{A22})$$

$$\hat{\rho} = \max\left(\rho_{\min}, \frac{D}{X\hat{W}}\right), \quad (\text{A23})$$

$$\hat{\epsilon} = \max\left(\epsilon_{\min}, \tau + D - \frac{S^r z}{\hat{W}}\right), \quad (\text{A24})$$

$$\hat{p} = \begin{cases} p(\hat{\rho}, \hat{\epsilon}) & \text{PF,} \\ p(\hat{\rho}, \hat{\epsilon}, \{\hat{Y}_i\}_i) & \text{MF,} \\ p^{\text{eq}}(\hat{\rho}, \hat{\epsilon}) + \hat{\Pi} & \text{HL and MC,} \end{cases} \quad (\text{A25})$$

where \hat{Y}_i and $\hat{\Pi}$ are³ computed implicitly in the conservative-to-primitive inversion. At the root of f , the quantities in Eqs. (A21)–(A25) correspond to the primitives, namely we can drop the hat, and $z = Wv$.

³ We also enforce $0 \leq \hat{Y}_i \leq 1$ and $-p^{\text{eq}} \leq \hat{\Pi} \leq p^{\text{eq}}$.

The minimal rest mass density is set to $\rho_{\min} = 10^{-20}$ and the minimal energy density ϵ_{\min} is obtained from ρ_{\min} and the cold EOS. Moreover, when the rest mass density obtained from the conservative-to-primitive inversion or from the reconstruction is smaller than the threshold value $\rho_{\text{thr}} = 100\rho_{\min}$, we set the primitive variables to their minimal values $\rho = \rho_{\min}, Wv = 0, u = \epsilon_{\min}/\rho_{\min} - 1, Y_i = 0, \Pi = 0$ (i.e., we set them to their atmosphere values).

The time derivatives in the source of Eqs. (30) and (31) are performed implicitly by including the advanced time quantity in the conservative-to-primitive inversion⁴. We computed implicitly also the terms containing the number reaction rates \mathcal{R}_i in Eq. (29) and the viscous timescale τ and the bulk stress Π in the right-hand side of Eqs. (30) and (31). Since the implicit terms are linear, a simple inversion is enough to recover the conservative variables when solving for Eq. (A18), while the implicit term is already known when solving for Eq. (A19). The spatial derivatives in the source of Eqs. (30) and (31) are performed explicitly (i.e., at the previous timestep), and are limited with the slope limiter. In order to avoid division by zero, we set a floor for the temperature at $T_{\min} = 10^{-61}$ (in code units) in the derivative in the source of the Hiscock-Lindblom equation [Eq. (30)], while χ is already limited by our choice of ρ_{\min} .

Appendix B: Tests

In this section we consider a set of standard tests for hydrodynamic codes in special and general relativity. Unless otherwise specified, we use the same code settings described in Sec. IV. In order to make a quantitative evaluation, we define the residual Δf of a quantity f as

$$\Delta f = \sum_{i=1}^N \frac{|f_i - \bar{f}_i|}{N}, \quad (\text{B1})$$

where the index i identifies the point in the grid of dimension N and \bar{f}_i is either the exact value or the value at the highest available resolution, according to the test.

In the following, we use 3rd order IMEX-RK with CFL = 0.5, 2nd order spatial reconstruction with MINMOD limiter, and the LLF Riemann solver.

1. Special-relativistic shocktube

The shocktube is a one dimensional problem where two different thermodynamic states of a fluid are initially sep-

⁴ Note that Chabanov et al. [50] performed an equivalent time derivative in the source term with a two-step predictor-corrector time evolution (Eq. (106) of Chabanov et al. [50]).

arated by a wall, which is lifted at $t = 0$. The hydrodynamic equations are:

$$\partial_t D + \partial_x (Dv) = 0, \quad (\text{B2})$$

$$\partial_t S^x + \partial_x (S^x v + p) = 0, \quad (\text{B3})$$

$$\partial_t \tau_\epsilon + \partial_x (S^x - Dv) = 0, \quad (\text{B4})$$

where $D = \rho W$, $S^x = (\epsilon + p)W^2 v$, and $\tau_\epsilon = (\epsilon + p)W^2 - p - D$.

We use an evenly spaced Cartesian grid from $x = 0$ to $x = 1$ with varying size $N = \{100, 200, 400, 800\}$, constant values of the primitives in the ghost cells, and the ideal EOS:

$$p = (\Gamma - 1)\rho u, \quad (\text{B5})$$

with $\Gamma = 4/3$. The fluid is initialized in a rarefaction-shock configuration: $\rho(x < 0.5) = 0.9$, $\rho(x > 0.5) = 0.1$, $p(x < 0.5) = 1$, $p(x > 0.5) = 0.001$, and $v = 0$. In Fig. 8 we plot the result of the test at $t = 0.35$. The residuals with respect to the exact solution decrease increasing the grid size, as expected, which proves the convergence of the code. The order of convergence is smaller than the nominal order of our code (which is second order), because of the presence of the shock.

2. Bjorken flow

The Bjorken flow describes the quark-gluon plasma in the center-of-mass of an ultra-relativistic heavy-ion collision [51]. This is a standard test for viscous codes describing heavy-ion collisions [52], and it has been used also in an astrophysical context by Chabanov et al. [50]. Only in this section, we use the Milne coordinates:

$$d\tilde{t}^2 = -dt^2 + t^2 dx^2, \quad (\text{B6})$$

where $\tilde{t} = t \cosh x$ and $\tilde{x} = t \sinh x$ are the time and spatial coordinates in the Minkowski spacetime. The determinant of the metric is $\sqrt{-g} = t$ and the only nonzero connection coefficients are $\Gamma_{xx}^t = t$ and $\Gamma_{xt}^x = \Gamma_{tx}^x = t^{-1}$. In the boosted system the velocity is null and therefore we have $v = 0$, $W = 1$, $u^\mu = (1, 0)$, and $T^{\mu\nu} = \text{diag}(\epsilon, (p^{\text{eq}} + \Pi)/t^2)$. Also, there are no spatial fluxes; the hydrodynamic equations therefore read (see also Sec. 3.4 of Del Zanna et al. [52]):

- continuity equation:

$$\partial_t(\rho t) = 0, \quad (\text{B7})$$

- since there are no fluxes the momentum conservation equation is trivial,
- energy conservation equation:

$$\partial_t \epsilon = -\frac{\epsilon + p^{\text{eq}}(\rho, \epsilon) + \Pi}{t}, \quad (\text{B8})$$

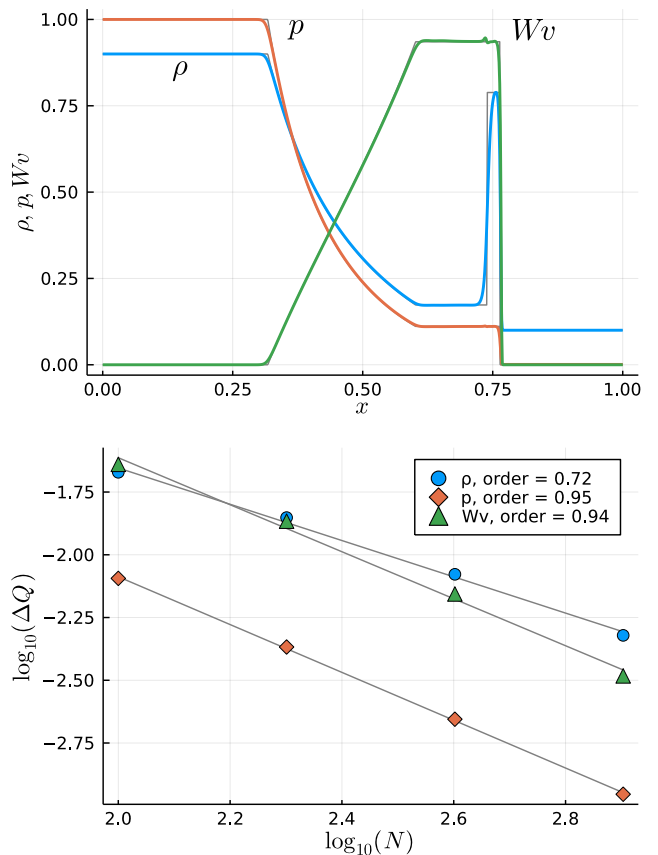


FIG. 8: Result of the relativistic shocktube test at $t = 0.35$. On the top, we plot the rest mass density ρ (light blue), pressure p (orange), and the Lorentz factor times the velocity Wv (green), for the grid size $N = 800$, against the exact solution (gray). On the bottom, we plot the residual of the same quantities with respect to the exact solution as a function of the grid size and report the convergence order in the legend for each of them.

- bulk stress evolution in Hiscock-Lindblom theory:

$$\partial_t(t\Pi) = -\frac{t\Pi}{2} \left(\frac{2}{\tau} - \frac{1}{t} + \partial_t \log \frac{\chi}{T^{\text{eq}}} \right) - \frac{1}{\chi}, \quad (\text{B9})$$

- bulk stress evolution in Maxwell-Cattaneo theory:

$$\partial_t(t\Pi) = -t\Pi \left(\frac{1}{\tau} - \frac{1}{t} \right) - \frac{1}{\chi}. \quad (\text{B10})$$

For constant χ and τ the Maxwell-Cattaneo equation (B10) has the analytical solution [52]:

$$\Pi(t) = \Pi(t_0) e^{-\frac{t-t_0}{\tau}} + \frac{\zeta}{\tau} e^{-t/\tau} (\text{Ei}(t_0/\tau) - \text{Ei}(t/\tau)), \quad (\text{B11})$$

where t_0 is the initial time and Ei the exponential integral function.

We use the following EOS [41]:

$$u(\rho, s) = k_0 \rho^{\Gamma-1} + k_{\text{th}} s^2 \rho^{\Gamma_{\text{th}}-1}, \quad (\text{B12})$$

with $\Gamma = 2, \Gamma_{\text{th}} = 1.75, k_0 = 100, k_{\text{th}} = 1.5$. The initial time is $t_0 = 1$, the initial rest mass density $\rho(t_0) = \rho_n$, the initial entropy $s(t_0) = 10$, the initial bulk stress $\Pi(t_0) = 10^{-8}$, the bulk parameter and bulk timescales are the constant values $\chi = 100/\rho_n$ and $\tau = 1$, and the timestep is $dt = \text{CFL} \times 0.1$. We evolve implicitly the terms containing the viscous timescale τ , the bulk stress Π , and the time derivative in the right-hand side of Eqs. (B9) and (B10). In Fig. 9 we plot the results of the simulations. The Maxwell-Cattaneo equation [Eq. (B10)] reproduces very well the exact solution [Eq. (B11)], while the Hiscock-Lindblom equation [Eq. (B9)] has the same trend of the Maxwell-Cattaneo case but differs from it, because the second order effects are important in the Bjorken flow. The solution for the Hiscock-Lindblom equation is closer to local thermodynamic equilibrium (i.e., the absolute value of the bulk stress is smaller) than the Maxwell-Cattaneo equation. This is similar to what happens in viscous cosmological models (see Eq. (5) of Maartens [53]). During the evolution, the pressure remains greater of the magnitude of the bulk stress, but due to the expansion of the Bjorken flow it decreases with time and $|\Pi| \rightarrow p$, at which point the viscous approximation is no more valid.

3. General-relativistic dust collapse

The dust collapse (also called Oppenheimer-Snyder collapse) is the gravitational collapse in spherical coordinates of an initially homogeneous pressure-less fluid. The exact solution for the general relativistic dust collapse in radial gauge, polar slicing coordinates was determined by Petrich et al. [54] (see also the Appendix of Romero et al. [40]).

We use the pressure-less EOS given by

$$\epsilon(\rho) = \rho, \quad (\text{B13})$$

and set $p = \mathcal{Q} = 0$ in Eqs. (23)–(28). In Fig. 10 we show the results at times $t = \{30, 40, 50\}$ for an initially homogeneous configuration of total gravitational mass $M = 1$ and initial radius $R(t = 0) = 10$; we consider the different grid resolutions $N = \{100, 200, 400, 800\}$, the maximal grid radius is $R_{\text{max}} = 13$, and the timestep is $dt = \text{CFL} \times dr$. The simulation follows the exact solution for most of the evolution, but (i) there is a buildup of material close to the origin, as noticed also by O’Connor and Ott [39], (ii) the surface of the collapsing cloud is smeared out (note that the velocity tail corresponds to a vanishing density), as noticed also by Romero et al. [40], and (iii) at late times the simulation starts diverging from the exact solution. In any case, the code converges to the exact solution increasing the resolution (see plots (c) and (d) of Fig. 10), even if the order of convergence is lower than 1. These inaccuracies are due to the steep spatial and temporal gradients that develop in the simulation.

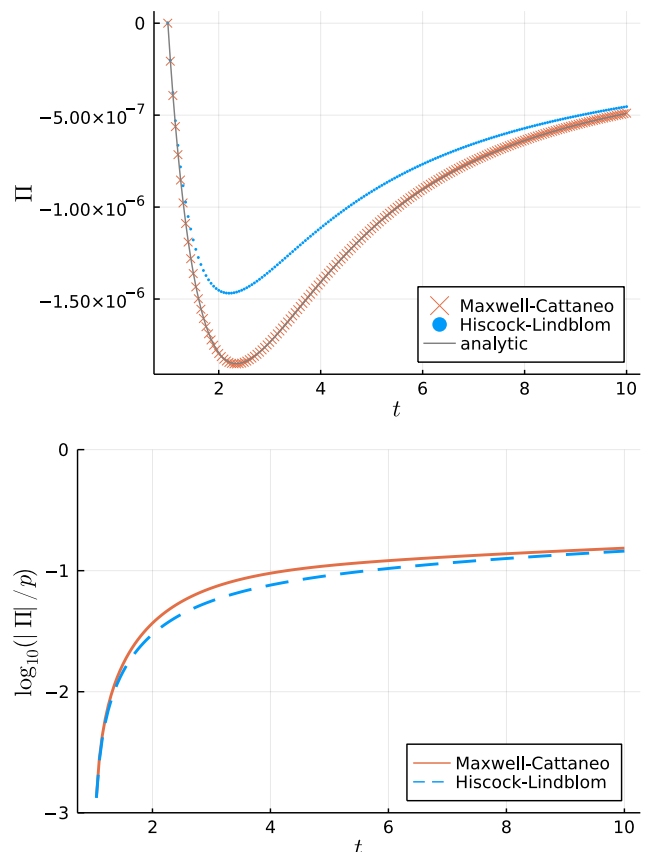


FIG. 9: Bjorken flow. On the top, we plot the bulk stress Π , on the bottom, the logarithm of the absolute value of the bulk stress over the pressure $|\Pi|/p$. We compare the evolution of the Hiscock-Lindblom equation (Eq. (B9), blue dots in the top figure and blue dashed line in the bottom figure) and the Maxwell-Cattaneo equation (Eq. (B10), orange crosses in the top figure and orange solid line in the bottom figure), for which it does exist an analytic solution (Eq. (B11), gray solid line in the top figure).

4. Neutron star oscillations

The hydrodynamic equation for this test are Eqs. (23)–(28) with $\mathcal{Q} = 0$. We use the ideal EOS [Eq. (B5)] with $\Gamma = 2$. The initial configuration is a cold spherical solution of the TOV equations with central density $\rho_0 = 1.28 \times 10^{-3}$, initialized with the cold EOS:

$$p(\rho) = k_0 \rho^\Gamma, \quad (\text{B14})$$

with $k_0 = 100$, and we set an initial velocity perturbation $v(r) = v_{\text{pert}} \times \sin(\pi r/R)$, where $v_{\text{pert}} = 5 \times 10^{-3}$ (unless otherwise specified) and R is the stellar radius. We consider 4 different resolutions for the grid: $N = \{100, 200, 400, 800\}$, we set $R_{\text{max}} = 11$, and we end the evolution at $t_{\text{end}} = 20$ ms.

We show the results in Table V and Fig. 11. We obtain the spectrum of the radial oscillations by Fourier-transforming the cosine-tapered (with a 5% taper ratio)

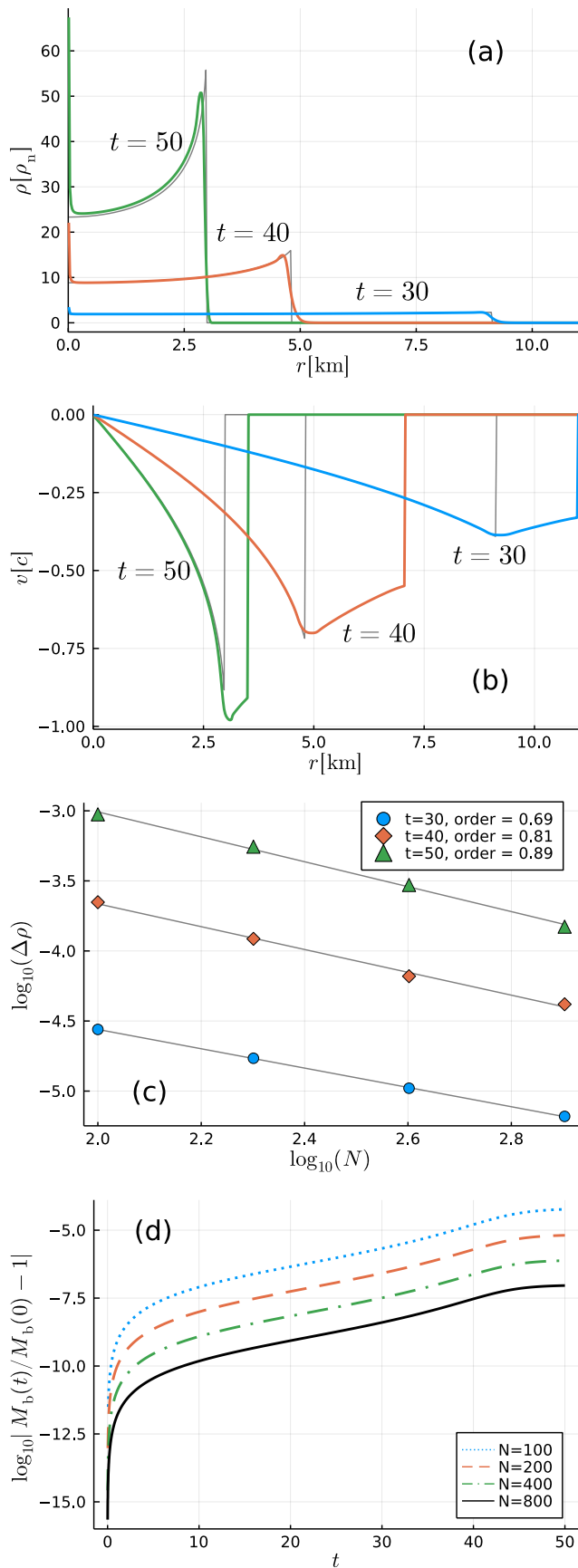


FIG. 10: Pressure-less dust collapse at times $t = 30, 40, 50$. From top to the bottom: density (a) and velocity (b) profiles at grid resolution $N = 800$ against the exact solution (gray line); residual of the rest mass density with respect to the exact solution (c), and the total rest mass variation during the evolution (d).

TABLE V: Frequencies of the first 3 radial modes, gravitational mass, and maximal variation of the absolute value of the baryonic mass for the different resolutions, compared with the result from perturbation theory (last row, see Tables I and II of Baiotti et al. [55]). Since we are evolving the star for $t = 20$ ms, the Fourier spectrum has a resolution of $\delta f = 50$ Hz.

N	$f_0[\text{Hz}]$	$f_1[\text{Hz}]$	$f_2[\text{Hz}]$	$M[M_\odot]$	$\max \Delta M_b/M_b(t=0) $
100	1450	3850	5750	1.40	4.3×10^{-8}
200	1450	3900	5850	1.40	4.8×10^{-9}
400	1450	3950	5900	1.40	5.7×10^{-10}
800	1450	3950	5900	1.40	6.9×10^{-11}
-	1462	3938	5928	1.40	-

signal obtained by interpolating (after subtracting a linear fit) the central density on an evenly spaced time grid with the same number of points of the original one. As expected, (i) the frequencies of the first 3 radial oscillation modes converge within the uncertainty to the results from perturbation theory [55] with increasing resolution, (ii) the gravitational mass is the same expected from the spherical solution, (iii) the central rest mass density oscillates around the initial value during the simulation, and (iv) the maximal deviation from the initial total rest mass decreases with increasing resolution. In order to study how the residual changes with the resolution, we have set $v_{\text{pert}} = 0$ and we have computed the residual of the rest mass density at $t = 20$ ms with respect to the initial configuration. The convergence of the residual is closer to the expected 2nd order than in the other test cases, since the oscillation is a smooth problem.

5. Migration from unstable to stable branch

For this test we use the same hydrodynamic equation and EOS of Sec. B 4, but the initial central rest mass density is $\rho_0 = 7.993 \times 10^{-3}$, corresponding to a gravitational mass $M \simeq 1.45$ and an initial circumferential radius $R \simeq 5.8$ [56–58].

We set $R_{\text{max}} = 80$ and consider different grid resolutions $dr = \{0.08, 0.04, 0.02, 0.01\}$, which are equivalent to $N = \{1001, 2001, 4001, 8001\}$. We show the results in Fig. 12. The migration causes a series of shock waves at the surface of the neutron star that eject material that eventually reach the computational grid at a time greater than ~ 1.6 ms. For this reason, in Fig. 12 we show the profile and the residuals at 1.5 ms, and the mass conservation is considered only up to 1.5 ms, while the central density oscillations are shown up to 5 ms since they are less affected by what happens close to the external grid border (at 5 ms the density at the external grid point is of the order $\sim 10^{-8}$). The final result of the oscillation is the configuration considered in Appendix B 4, but (i) part of the gravitational mass is converted into kinetic energy and (ii) due to the shocks at the surface part of

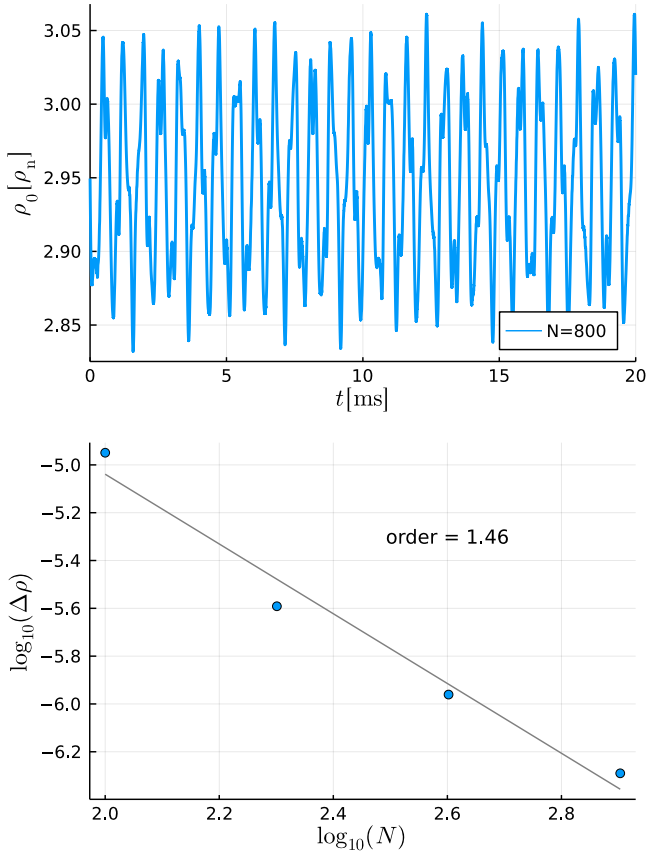


FIG. 11: Neutron star oscillations. On the top, the evolution of the central rest mass density. On the bottom, the residuals at the end of the evolution (20 ms) for different resolutions and for $v_{\text{pert}} = 0$.

the material is ejected. The code converges with the resolution with an order smaller than 1 because there are strong shocks at the surface of the neutron star.

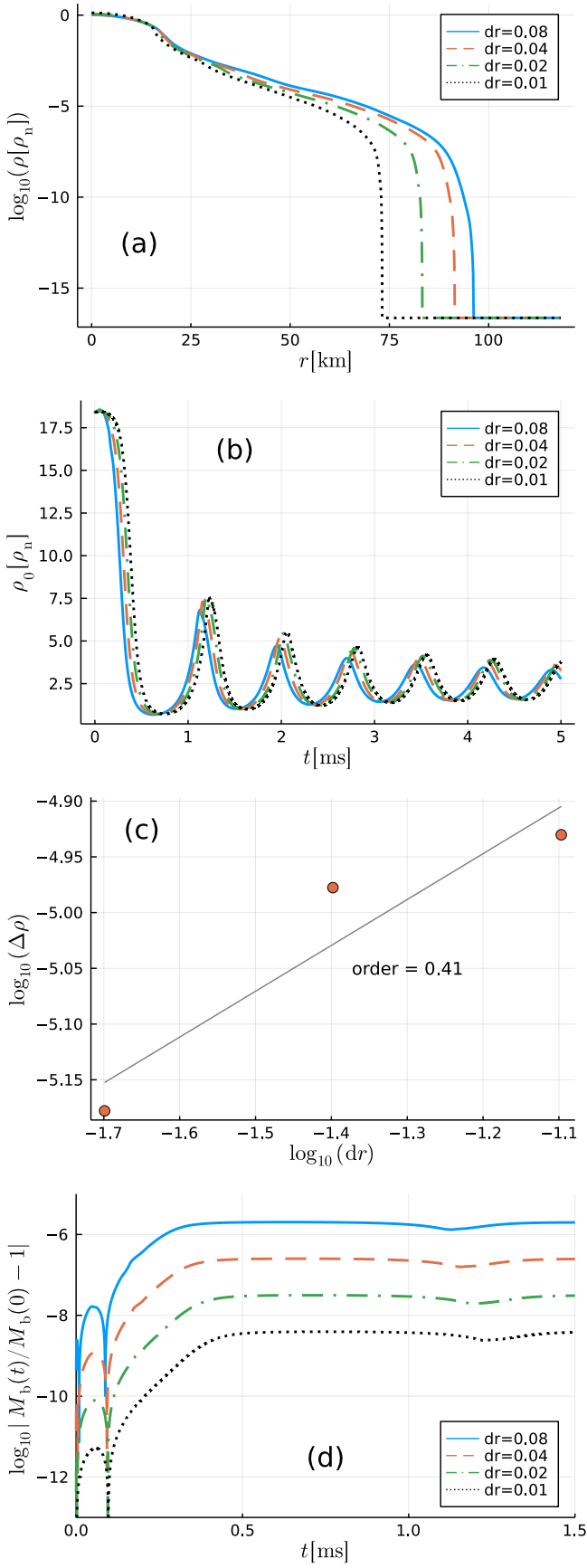


FIG. 12: Migration from unstable to stable branch. From top to bottom: (a) profile of the rest mass density at 1.5 ms, (b) central rest mass density evolution up to 5 ms, (c) residual at 1.5 ms with respect to the maximum resolution, and (d) baryon mass conservation up to 1.5 ms.